The Astrophysical Journal Supplement Series, 206:8 (19pp), 2013 May doi:10.1088/0067-0049/206/1/8

A PUBLIC K_s-SELECTED CATALOG IN THE COSMOS/ULTRAVISTA FIELD: PHOTOMETRY, PHOTOMETRIC REDSHIFTS, AND STELLAR POPULATION PARAMETERS*,†

Adam Muzzin[1], Danilo Marchesini[2], Mauro Stefanon[3], Marijn Franx[1], Bo Milvang-Jensen[4], James S. Dunlop[5], J. P. U. Fynbo[4], Gabriel Brammer[6], Ivo Labbé[1], and Pieter van Dokkum[7]
[1] Leiden Observatory, Leiden University, P.O. Box 9513, 2300 RA Leiden, The Netherlands
[2] Department of Physics and Astronomy, Tufts University, Medford, MA 06520, USA
[3] Physics and Astronomy Department, University of Missouri, Columbia, MO 65211, USA
[4] Dark Cosmology Centre, Niels Bohr Institute, University of Copenhagen, Juliane Maries Vej 30, DK-2100 Copenhagen, Denmark
[5] SUPA, Institute for Astronomy, University of Edinburgh, Royal Observatory, Edinburgh EH9 3HJ, UK
[6] European Southern Observatory, Alonso de Córdova 3107, Casilla 19001, Vitacura, Santiago, Chile
[7] Department of Astronomy, Yale University, New Haven, CT 06520-8101, USA
Received 2013 March 11; accepted 2013 April 8; published 2013 May 3

ABSTRACT

We present a catalog covering 1.62 deg^2 of the COSMOS/UltraVISTA field with point-spread function (PSF) matched photometry in 30 photometric bands. The catalog covers the wavelength range 0.15–24 μm including the available *GALEX*, Subaru, Canada–France–Hawaii Telescope, VISTA, and *Spitzer* data. Catalog sources have been selected from the DR1 UltraVISTA K_s band imaging that reaches a depth of $K_{s,\mathrm{tot}} = 23.4$ AB (90% completeness). The PSF-matched catalog is generated using position-dependent PSFs ensuring accurate colors across the entire field. Also included is a catalog of photometric redshifts (z_{phot}) for all galaxies computed with the EAZY code. Comparison with spectroscopy from the zCOSMOS 10k bright sample shows that up to $z \sim 1.5$ the z_{phot} are accurate to $\Delta z/(1+z) = 0.013$, with a catastrophic outlier fraction of only 1.6%. The z_{phot} also show good agreement with the z_{phot} from the NEWFIRM Medium Band Survey out to $z \sim 3$. A catalog of stellar masses and stellar population parameters for galaxies determined using the FAST spectral energy distribution fitting code is provided for all galaxies. Also included are rest-frame $U-V$ and $V-J$ colors, L_{2800} and L_{IR}. The *UVJ* color–color diagram confirms that the galaxy bi-modality is well-established out to $z \sim 2$. Star-forming galaxies also obey a star-forming "main sequence" out to $z \sim 2.5$, and this sequence evolves in a manner consistent with previous measurements. The COSMOS/UltraVISTA K_s-selected catalog covers a unique parameter space in both depth, area, and multi-wavelength coverage and promises to be a useful tool for studying the growth of the galaxy population out to $z \sim 3$–4.

Key words: galaxies: evolution – galaxies: fundamental parameters – galaxies: high-redshift – infrared: galaxies

Online-only material: color figures

1. INTRODUCTION

The last decade has seen significant progress in our understanding of the evolution of massive galaxies ($\log(M_{\mathrm{star}}/M_\odot) > 11.0$) at $0 < z < 5$. These galaxies already exist in significant numbers at $2 < z < 5$, and their number density evolves fairly quickly over this redshift range (e.g., McLure et al. 2006; Marchesini et al. 2009, 2010; Cirasuolo et al. 2010; Caputi et al. 2011). This early and rapid formation of massive galaxies is not well-reproduced in current theoretical models where high-mass galaxies typically form much later (e.g., Fontanot et al. 2009; Guo et al. 2011; Henriques et al. 2012; Bower et al. 2012).

Between $0 < z < 2$ the growth of massive galaxies is more gradual (e.g., Bundy et al. 2006; Arnouts et al. 2007; Marchesini et al. 2009; Ilbert et al. 2010; Brammer et al. 2011; Bielby et al. 2012), perhaps because this redshift range is also marked by a significant decrease in the star formation rates of these galaxies. Current data show that the bi-modality between quiescent galaxies and star-forming galaxies is largely established between $1 < z < 2$ (e.g., Williams et al. 2009; Whitaker et al. 2011; Brammer et al. 2011). Below $z < 1$, it appears the transformation of massive star-forming galaxies into massive quiescent galaxies is largely completed and any subsequent mass growth in the massive population is primarily driven by mergers (e.g., Bundy et al. 2006; Arnouts et al. 2007; Ilbert et al. 2010; Brammer et al. 2011).

This impressive recent progress in measuring the evolution of massive galaxies has primarily been made possible by the extensive investments made in ground-based near-infrared (NIR) imaging capabilities over the last decade. The early deep pencil-beam NIR surveys that allowed for the first identifications of massive, high-redshift galaxies (e.g., Franx et al. 2003; Förster Schreiber et al. 2004; Daddi et al. 2005; van Dokkum et al. 2006) such as FIRES (0.002 deg^2; Labbé et al. 2003), GOODS (0.04 deg^2; Wuyts et al. 2008), and MUSYC (0.12 deg^2; Quadri et al. 2007), have now been superceded by much wider surveys that are equivalently deep, or deeper. These surveys, such as the NEWFIRM Medium Band Survey (NMBS; 0.44 deg^2; van Dokkum et al. 2009; Whitaker et al. 2011), the UKIDSS-UDS (0.7 deg^2; Lawrence et al. 2007; Williams et al. 2009), and WIRDS (2.1 deg^2; McCracken et al. 2010; Bielby et al. 2012) are now the best-studied cosmic windows onto the massive galaxy population and have provided the source data for most of the results previously mentioned.

The latest in this series of wider and deeper NIR sky surveys is the UltraVISTA survey (McCracken et al. 2012). UltraVISTA has imaging in four broad-band NIR filters ($YJHK_s$) as well as one narrow-band filter centered on Hα at $z = 0.8$ (NB118).

* Based on data products from observations made with ESO Telescopes at the La Silla Paranal Observatory under ESO program ID 179.A-2005 and on data products produced by TERAPIX and the Cambridge Astronomy Survey Unit on behalf of the UltraVISTA consortium.
† Catalog and other data products are available at http://www.strw.leidenuniv.nl/galaxyevolution/ULTRAVISTA/.

Table 1
Summary of Photometric Data

Filter (1)	FWHM Seeing (″) (2)	5σ Depth (2.″1) (3)	Reference (4)
FUV	4.35.	25.2	Martin et al. (2005)
NUV	4.65.	25.1	...
u^*	0.82–0.89	26.6–26.9	Capak et al. (2007)
B_j	0.71–0.78	26.8–27.1	...
g^+	1.01–1.20	26.3–26.5	...
V_j	0.74–0.84	26.2–26.4	...
r^+	0.78–0.85	26.2–26.4	...
i^+	0.53–0.68	25.9–26.1	...
z^+	0.81–0.91	25.0–25.3	...
IA427	0.66–0.75	26.1–26.2	...
IA464	0.78–1.05	25.8–25.9	...
IA484	0.54–0.72	26.1–26.2	...
IA505	0.71–0.84	25.8–26.0	...
IA527	0.59–0.67	26.1–26.2	...
IA574	0.87–0.94	25.7–25.8	...
IA624	0.70–0.81	25.8–26.0	...
IA679	0.87–1.02	25.5–25.7	...
IA709	0.76–0.90	25.7–25.9	...
IA738	0.72–0.80	25.6–25.7	...
IA767	0.98–1.07	25.3–25.5	...
IA827	0.90–1.08	25.4–25.5	...
Y	0.82–0.86	24.3–24.6	McCracken et al. (2012)
J	0.81–0.85	24.2–24.4	...
H	0.78–0.82	23.8–24.1	...
K_s	0.77–0.82	23.7–23.9	...
3.6 μm	1.75	23.9	Sanders et al. (2007)
4.5 μm	1.78	23.3	...
5.8 μm	1.99	21.3	...
8.0 μm	2.24	21.0	...
24 μm	5.91	45 μJy	...

Notes. Seeing information is the full range of seeing from an average of 10 PSF stars in each of the 9 subfields. The depths within the 2.″1 aperture are on the PSF-matched images and hence are effective depths for the purpose of color measurements in the catalog. The quoted depth at 24 μm is a total flux.

UltraVISTA is the deepest of the VISTA public surveys, and when fully complete will cover an area of 1.8 deg^2 down to $K_s \sim 24.0$, with a deeper component (referred to as "ultra-deep") covering 0.75 deg^2 down to $K_s \sim 25.6$ (see McCracken et al. 2012). The current first data release of UltraVISTA is based on approximately one season of observing time and is now publicly available (McCracken et al. 2012). In those data the imaging reaches a 5σ depth of $K_s < 23.9$ AB in a 2″ aperture. The full-depth UltraVISTA data set will be acquired over a period of 5–7 years.

In addition to a unique combination of area and depth, one of the main strengths of UltraVISTA is that the survey field is the COSMOS field (Scoville et al. 2007). COSMOS has arguably the most impressive array of multiwavelength coverage of any degree-scale part of the sky. It contains X-ray data from *XMM-Newton* (Hasinger et al. 2007) and *Chandra* (Elvis et al. 2009), UV imaging from the *GALEX* satellite (Martin et al. 2005), extensive optical broad-band and optical medium-band imaging from the Canada–France–Hawaii Telescope (CFHT) and Subaru telescope (Taniguchi et al. 2007; Capak et al. 2007), mid-infrared data from *Spitzer* (Sanders et al. 2007; Frayer et al. 2009), submillimeter data from *Herschel* (Oliver et al. 2012), millimeter data from AzTEC and MAMBO (Scott et al. 2008; Aretxaga et al. 2011), as well as radio observations from the Very Large Array (Schinnerer et al. 2007, 2010). The field also has spectroscopy for ∼25,000 galaxies from the zCOSMOS-bright (Lilly et al. 2007, 2009) and zCOSMOS-deep surveys (Lilly et al. 2007). In addition to this, it also has *Hubble Space Telescope* (*HST*) Advanced Camera for Surveys (ACS) data (Koekemoer et al. 2007) covering the full field as well as deep WFC3 NIR imaging in part of the field from the CANDELS survey (Grogin et al. 2011; Koekemoer et al. 2011), and additional WFC3 imaging and grism spectroscopy from the 3D-HST survey (Brammer et al. 2012). This extensive multi-wavelength coverage makes COSMOS an attractive field for performing studies of distant galaxies.

In this paper we present and make available a 30 band photometric catalog of the COSMOS field covering the wavelength range 0.15–24 μm. The selection of sources has been made using the high image quality UltraVISTA K_s-band which allows for efficient selection of mass-complete samples of galaxies up to $z = 4$. In addition to the photometric catalog, we also make available a catalog of photometric redshifts, stellar population parameters, rest-frame colors, and UV/IR luminosities for all galaxies in the survey. The stellar mass function of galaxies to $z = 4$ determined using this catalog is presented in a companion paper (Muzzin et al. 2013).

The layout of this paper is as follows. In Section 2 we discuss the various observational data sets included in the photometric catalog. In Section 3 we outline the steps of the catalog creation such as the point-spread function (PSF) matching, source detection, and data quality controls. In Section 4 we present the catalog of photometric redshifts and compare these to other photometric and spectroscopic redshift measurements. In Section 5 we present a catalog of stellar population parameters, and examine the basic properties of galaxies in the catalog such as the galaxy bi-modality and star formation "main sequence." We conclude with a summary in Section 6. Throughout this paper we assume an $\Omega_\Lambda = 0.7$, $\Omega_m = 0.3$, and $H_0 = 70$ km s^{-1} Mpc^{-1} cosmology. All magnitudes are in the AB system.

2. DESCRIPTION OF THE DATA SET

2.1. Photometric Data Sets

There is a wealth of imaging data at various wavelengths available for the COSMOS field. For the K_s-selected catalog we have chosen to include 30 photometric bands that cover the wavelength range 0.15–24 μm. These bands and the papers that describe these data sets are summarized in Table 1.

The catalog is based on the $YJHK_s$ NIR imaging data from UltraVISTA (McCracken et al. 2012), and the inclusion or exclusion of the available data sets was chosen to provide a match in areal coverage and depth of those data. The optical data consist of broad-band data taken with Subaru/SuprimeCam ($g^+r^+i^+z^+B_jV_j$), as well as u^* data from the CFHT/MegaCam (Taniguchi et al. 2007; Capak et al. 2007). We have also included the 12 optical medium bands (IA427–IA827) from Subaru/SuprimeCam (Capak et al. 2007) for a total of 23 optical/NIR bands. Observations from the *GALEX* FUV and NUV channels (see Martin et al. 2005), as well as the 3.6 μm, 4.5 μm, 5.8 μm, 8.0 μm, and 24 μm channels from *Spitzer*'s IRAC+MIPS cameras (see Sanders et al. 2007) have also been included using a source-fitting technique designed for determining robust colors in highly blended imaging data (see Section 3.5).

Several data sets have not been incorporated into the catalog. These include the deep $u^*g'r'i'z'$ imaging taken as part of the CFHTLS-Deep survey. These data are deeper than the

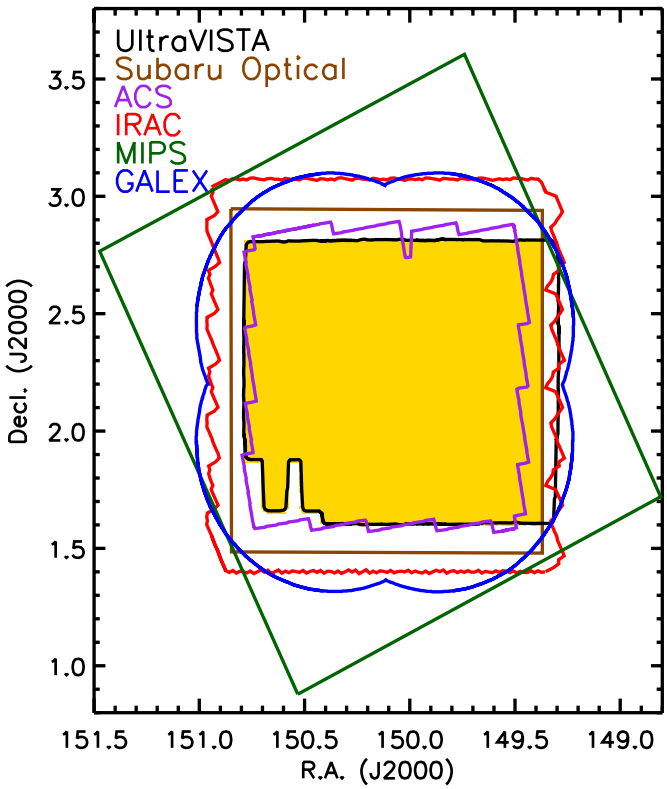

Figure 1. Coverage diagram for the UltraVISTA/COSMOS field. The filled gold region shows the area covered by the K_s-selected catalog. The catalog contains objects only in regions where both NIR and optical coverage is available. It covers a total of 1.62 deg^2, when regions contaminated by bright stars are excluded.

(A color version of this figure is available in the online journal.)

Subaru broad-band data; however, they cover ∼0.9 deg^2 near the center of the COSMOS field, which is only slightly more than half of the UltraVISTA area. In principle, these data should improve the quality of the photometric redshifts and stellar mass measurements for galaxies in that region of the survey; however, including them would cause the uncertainties in those quantities to be location-dependent. This makes it much more difficult to estimate uncertainties in quantities derived from the entire survey such as the stellar mass function or the color distribution of galaxies. For the same reason we have chosen not to include the deep NIR medium-band imaging from the NMBS (Whitaker et al. 2011), which covers only 0.22 deg^2 of the field.

We have also not included the *J*-band imaging of COSMOS from KPNO (Capak et al. 2007), or the *H* and K_s imaging from CFHT/WIRCAM (McCracken et al. 2010). Those data have full coverage of the field; however, they use similar filters as those in UltraVISTA and are shallower.

2.2. Field Geometry

The geometry of the COSMOS field is roughly a square patch on the sky; however, the coverage from the various data sets does not overlap perfectly. In Figure 1 we plot a schematic view of the layout of the data sets used in the photometric catalog. The selection band for the catalog is the UltraVISTA K_s-band which is shown as the black outline in Figure 1. The UltraVISTA full field covers ∼1.8 deg^2; however, as Figure 1 shows, it is placed slightly to the west of the centroid of the Subaru broad- and medium-band imaging (orange outline). This offset in the UltraVISTA field was necessary to ensure that the four "strips" that are observed as part of the ultra-deep component of UltraVISTA did not coincide with the positions of bright stars. The effective area of overlap between the Subaru optical data and the UltraVISTA NIR data is 1.62 deg^2 once bright stars have been masked, and this region is shown as the gold shaded region in Figure 1. All sources in the catalog are contained within this overlap region.

As Figure 1 shows, there is complete coverage for the 1.62 deg^2 catalog region from *GALEX*, IRAC, and MIPS. The majority of the ACS coverage is also within the UltraVISTA area.

3. PHOTOMETRY AND SOURCE DETECTION

Measuring the colors of galaxies accurately is paramount for determining properties such as photometric redshifts and stellar masses. The available imaging data in the COSMOS/UltraVISTA field comes with a wide range of PSF shapes and sizes and these variations need to be accounted for in the color measurements. The range of image qualities for the various filters is listed in Table 1 (see also Capak et al. 2007). As Table 1 shows, the image quality ranges from as good as 0.″5 FWHM in some of the optical bands, to as poor as 4″–5″ FWHM in the *GALEX* and MIPS 24 μm imaging. The optical and NIR imaging have PSFs that are comparable in shape (i.e., roughly Gaussian) and FWHM (0.″5–1.″2) and therefore PSF matching of those bands is performed in a similar way using standard techniques (see Section 3.1). The space-based imaging from *GALEX*, IRAC, and MIPS have more complicated PSF shapes that have considerable wings, as well as a much larger FWHM. Photometry for those bands is performed separately using a source-fitting code designed to measure accurate photometry for highly blended sources and is described in Section 3.5.

3.1. Optical and NIR PSF Matching

PSF matching between the optical and NIR bands is performed by degrading the image quality of all bands to the image quality of the worst-seeing band. This process is performed separately in different regions of the survey. Region-dependent PSF matching is needed because full coverage of the COSMOS field required nine SuprimeCam pointings per filter (see Capak et al. 2007). The result of these multiple pointings is that in addition to the image-quality variations between filters, there are also image-quality variations from pointing-to-pointing within a given filter. The range of PSF FWHMs for each filter is listed in Table 1.

To perform the PSF matching we divided the survey into nine patches (labeled COSMOS-1–COSMOS-9) closely tied to the positions of the SuprimeCam pointings. We note that this approach does not account for intra-stack seeing variations in the NIR bands which are caused by the sparsely filled nature of the VIRCAM mosaic. The intra-stack PSF variations are of the order of a few hundredths of an arcsecond (see, e.g., McCracken et al. 2012), and hence are much smaller than the PSF differences between different bands.

Within each region, 10 bright, unsaturated reference PSF stars were chosen and co-added into a reference PSF for that filter/region. Stars have a range of colors, and therefore it was difficult to find PSF stars that were suitably bright but unsaturated from the $u^* \rightarrow K_s$ bands. This was dealt with by choosing one set of stars for the $u^* \rightarrow$ IA679 bands, and a separate set of stars for the IA738 $\rightarrow K_s$ bands. An additional set of PSF stars was chosen for the Subaru i^+ band. The i^+ imaging has superior image quality (∼0.″5) across the field, and

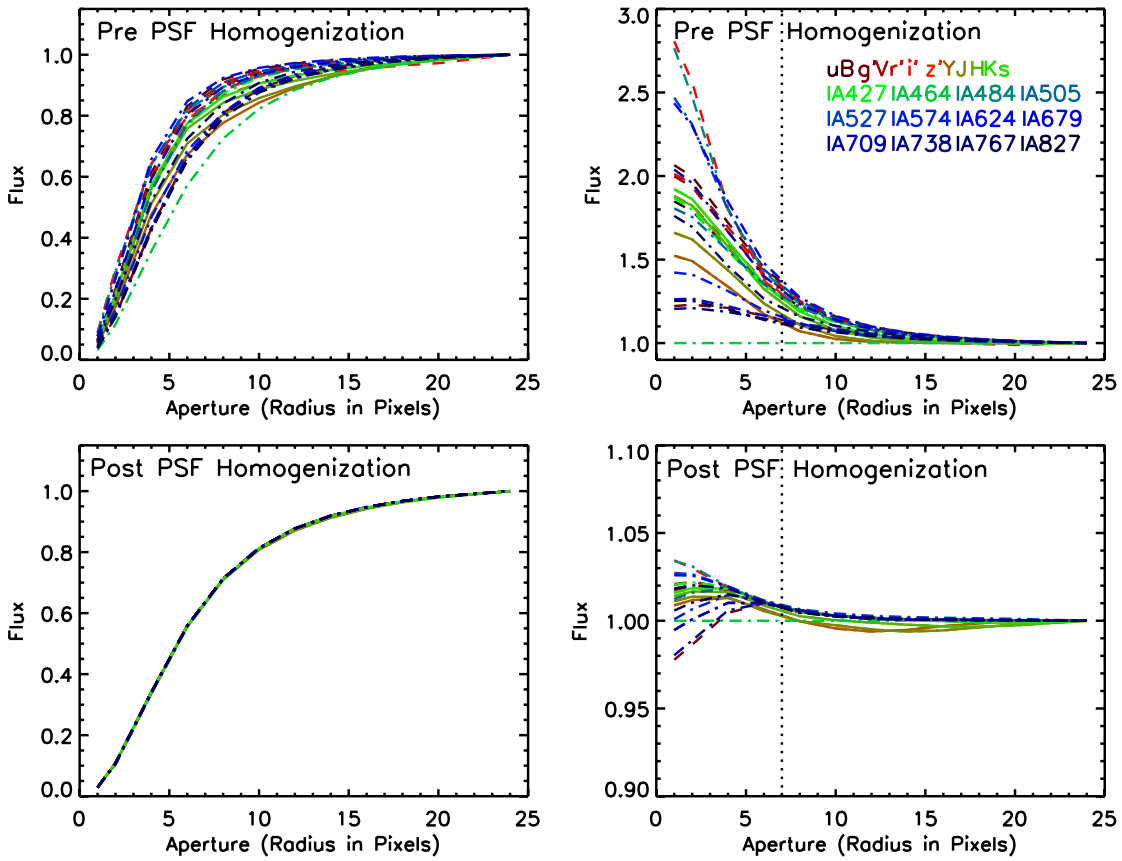

Figure 2. Top left: curve of growth for bright PSF stars in the field. Subaru optical broad bands (dashed lines), NIR bands (solid lines), and Subaru optical medium bands (dot-dashed lines) are shown. Top right: same curves of growth normalized relative to the worst seeing image (IA464, ∼1.″05). The color aperture is shown as the dotted vertical line. Bottom panels: same as top panels but after PSF homogenization has been performed. Before PSF homogenization, the range of fluxes within the color aperture is a factor of 1.4. After PSF homogenization, colors within the color aperture are accurate to ∼1%.

(A color version of this figure is available in the online journal.)

was taken with longer exposure times than the other bands so all stars down to $i^+ < 21.8$ are saturated (see also Capak et al. 2007). Finding unsaturated PSF stars required going to much fainter stars than in the other bands.

With a reference PSF constructed for each band/region we used the task `lucy` from the IRAF STSDAS package to compute the convolution kernels necessary to degrade the images to the image quality of the worst seeing band. In 2/9 of the regions the worst image-quality band was the IA464 band, with typical seeing of ∼1.″05. In the other 7/9 regions the worst image-quality band was the g^+ band with seeing of 1.″0–1.″2.

In Figure 2 we plot an illustration of the PSF matching process for the COSMOS-1 field. In the upper left panel we plot the growth curve of the PSF stars before PSF homogenization is performed. In the upper right panel we plot the same growth curves normalized relative to the worst seeing band (IA464). The dotted vertical line shows the 2.″1 aperture used for color measurements. Prior to PSF homogenization, the dispersion in the flux contained within the color aperture for the best and worst image-quality bands is a factor of ∼1.4.

In the bottom panels of Figure 2 we plot the reference stars after PSF homogenization has been performed. As the right panel shows, the dispersion in flux within the color aperture for the reference PSFs is reduced to <1%.

3.2. Source Extraction and Photometry

Source detection and photometry are performed using the SExtractor package (Bertin & Arnouts 1996) in dual image mode with the non-PSF-matched UltraVISTA K_s-band image as the detection image. Objects are detected by flagging pixels $>1.7\sigma$ above the background, after a 2 × 2 pixel convolution kernel has been applied. We require 10 connected pixels for a detection. At face-value this appears to be a conservative detection limit; however, it is required to prevent the detection of a significant number of spurious sources. The native pixel scale of VIRCAM is 0.″34 pixel^{-1} but the data have been resampled to the COSMOS optical data pixel scale of 0.″15 pixel^{-1} (see McCracken et al. 2012). This makes the noise in the UltraVISTA images highly correlated causing SExtractor to underestimate it and return a high fraction of spurious detections if a more relaxed object detection criterion is used.

Photometry is performed in each of the nine regions independently and afterward these are merged into a master catalog for the entire field. For each filter we determine two fluxes, a Kron-aperture flux based on SExtractor's `flux_auto` parameter, as well as the flux within a circular color aperture. The color aperture was chosen to be 14 pixels in diameter, corresponding to 2.″1 on the sky. This size makes the color aperture ∼2× the FWHM of the worst seeing image in each region.

For each galaxy we supply a total K_s-band magnitude ($K_{s,\mathrm{tot}}$) based on the `flux_auto` parameter from SExtractor. This flux is the flux measured within 2.5 times the Kron radius (R_K, Kron 1980). The measured flux within 2.5 × R_K should account for >96% of the total flux of the galaxy (Kron 1980). We correct the `flux_auto` to a total flux by measuring the growth curve

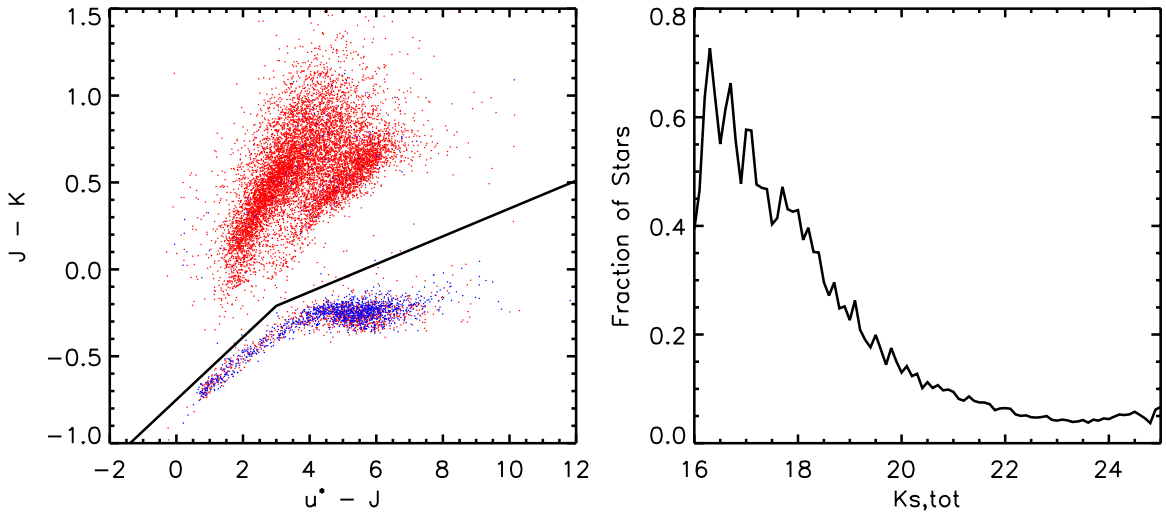

Figure 3. Left panel: the color–color space used to perform star/galaxy separation. One-third of objects with $K_s < 21.5$ are plotted. Objects that are classified as stars using SExtractor (`class_star` > 0.95) are plotted in blue and objects classified as galaxies (class_star <0.95) are plotted in red. There is a clear separation of stars and galaxies in the $u^* - J$ vs. $J - K_s$ color–color space. In the catalog, objects that lie below the lines are classified as stars, and those above are classified as galaxies. Right panel: fraction of objects that are stars as a function of K_s-band magnitude.

(A color version of this figure is available in the online journal.)

of bright stars out to a radius of 8″. Depending on the R_K, this correction is of the order 2%–4%, as expected.

In the catalog we remove all objects with magnitudes <3σ limit in the K_s-band ($K_s = 24.35$, 2.″1 aperture), which results in a final photometric catalog of 262,615 sources.

3.2.1. Galactic Extinction Correction

The photometry in all bands is corrected for Galactic dust attenuation using the dust maps from Schlegel et al. (1998). Dust extinctions are calculated in each of the nine photometry regions individually. The COSMOS field does not have substantial Galactic dust, and the corrections are of order 15% in the *GALEX* bands, 5% in the optical and <1% in the NIR and MIR.

3.2.2. Photometric Errors

All of the optical and NIR images have been resampled during the mosaicking process. The resampling causes correlations in the noise between pixels and therefore standard Poisson estimation of the background noise is not a reliable estimate of the photometric errors. We measure the background noise in each band, and in each region, by placing 10,000 empty apertures across the field and measuring the rms flux in those empty apertures. These rms estimates also give a measure of the 5σ depth for each filter, and we list those depths and the range of depths in Table 1. The quoted depths in Table 1 are the 5σ depth in the 2.″1 color aperture, and hence are the effective depth of the photometry. Given the uncertainty in the absolute IRAC zero point, we have also included an additional 5% systematic error to the IRAC magnitudes in quadrature.

Errors in $K_{s,\mathrm{tot}}$ are calculated using the method developed by Labbé et al. (2003), which was also used by Quadri et al. (2007) and Whitaker et al. (2011). The background noise in an aperture of diameter N pixels will scale as N^2 in the limiting case of perfect correlation between pixels, and will scale as N in the limiting case of no correlation between pixels. We parameterize the background noise in an aperture as $\sigma_{\mathrm{ap}} = \sigma_1 \alpha N^{\beta}$, where σ_1 is the size of the aperture in arcseconds, and $1 < \beta < 2$. We perform the empty-aperture measurement for a range of aperture sizes and fit this relation for α and β, finding $\beta = 1.82$ and $\alpha = -0.35$. From this relation we then compute the error in the `flux_auto` based on the rms noise in an aperture of 2.5 R_K.

3.3. Star Galaxy Separation

Similar to the NMBS, star galaxy separation is performed using the $J - K_s$ versus $u^* - J$ color space. In Figure 3 we plot this color space for a randomly selected subsample of 30% of the objects with $K_s < 21.5$. Points are color-coded by SExtractor's `class_star` parameter, with star-like profiles in blue and galaxy-like profiles in red. As Figure 3 shows, the two types of objects clearly segregate in color space. Based on this segregation, objects are classified as galaxies if they meet the following color criteria:

$$J - K_s > 0.18 \times (u^* - J) - 0.75, [u - J < 3.0], \quad (1)$$

$$J - K_s > 0.08 \times (u^* - J) - 0.45, [u - J > 3.0]. \quad (2)$$

As shown in the right panel of Figure 3, stars dominate the catalog at $K_{s,\mathrm{tot}} < 17$, but make up <10% of objects at $K_{s,\mathrm{tot}} > 21.0$.

3.4. Survey Completeness

In order to construct mass- or luminosity-limited samples, the completeness as a function of the selection band needs to be quantified. To estimate the point-source completeness we use the PSF stars as template sources, and insert these into the original non-PSF-matched K_s-band image. We then attempt to recover these sources with SExtractor. When recovering the simulated stars we used the same SExtractor parameters that were used for object detection in the catalog.

This completeness test is performed in two ways. First, we insert sources into a version of the image where all objects have been masked out using SExtractor's segmentation map and then attempt to recover these objects with SExtractor. The recovery rate of these objects gives an estimate of the completeness based solely on the noise properties of the image. We then perform the test again, this time using the real image with all objects still included. The recovery rate of this method gives a measure

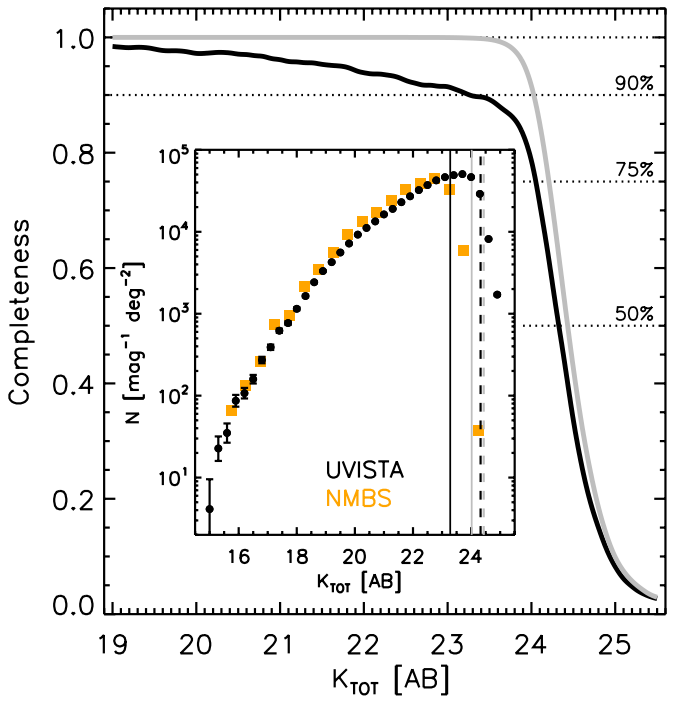

Figure 4. Completeness fraction as a function of total K_s-band flux for point sources. The completeness is calculated using simulations which insert point sources into the K_s-band image and attempt to recover them. The gray curve is calculated by masking all real sources in the image and demonstrates the completeness based on the background noise in the image. The black curve is calculated by keeping in all real sources and therefore is lower because of effects such as blending and confusion. In the inset we show the differential number counts in K_s-band and a comparison to the number counts from the NMBS (Whitaker et al. 2011). Based on the simulations and the inflection in the number counts, the 90% completeness limit of the catalog is $K_{s,\mathrm{tot}} < 23.4$.

(A color version of this figure is available in the online journal.)

of the overall completeness, which is always less than unity because of real effects that cause objects to be missed such as contamination from bright stars, or blending with other galaxies.

In Figure 4 we plot the completeness curves as a function of $K_{s,\mathrm{tot}}$. The 90% completeness limit in terms of the noise properties alone is $K_{s,\mathrm{tot}} = 24.0$ mag; however, this corresponds to <80% completeness in the real data. Based on the noise properties, the 100% completeness level of the UltraVISTA $K_{s,\mathrm{tot}}$ data is 23.4 mag. This $K_{s,\mathrm{tot}}$ limit corresponds to a 90% completeness level in the actual data. At magnitudes fainter than 23.4 the data become incomplete quite rapidly. This can be seen as the inflection point in the number counts in the inset of Figure 4 (see also McCracken et al. 2012), which is the result of increasing incompleteness as well as the increase in photometric uncertainties due to poor signal-to-noise (S/N) near the completeness limit. In order to construct mass-complete samples we only use sources in the catalog with $K_{s,\mathrm{tot}} \leqslant 23.4$. We note that this completeness is 0.08 mag *brighter* than would be measured using the DR1 UltraVISTA data from McCracken et al. (2012). We have adjusted the zero point of the DR1 images by this amount in order to bring it into better agreement with other K_s surveys such as the Two Micron All Sky Survey (2MASS) and the NMBS (see the Appendix).

Also shown in the inset of Figure 4 is the sample completeness measurement from the NMBS (Whitaker et al. 2011). The 90% completeness of the NMBS is $K_{\mathrm{tot}} < 22.8$, showing that UltraVISTA is ∼0.6 mag deeper than NMBS. The surveys have similar exposure times on 4 m class telescopes, so the extra depth is primarily a result of the superior image quality in the UltraVISTA DR1 (∼0.″75, McCracken et al. 2012) compared to the NMBS (∼1.″1, Whitaker et al. 2011).

3.5. IRAC and MIPS Photometry

The PSF FWHMs of IRAC and MIPS are approximately 2–5× larger than the FWHM of the worst seeing optical and NIR PSF FWHMs. This means that degrading the image quality of the optical/NIR data to that image quality would cause a substantial reduction in the S/N of the color measurements as well as unnecessary blending of well-resolved galaxies. Therefore, instead of degrading PSFs we use a source-fitting code developed to measure deblended photometry of heavily confused images. This code is well-tested and has been used in many previous K_s-selected catalogs (see Labbé et al. 2005; Wuyts et al. 2007; Marchesini et al. 2009; Williams et al. 2009; Whitaker et al. 2011; Marchesini et al. 2012), including several with ultra-deep IRAC imaging (Labbé et al. 2010; Labbé et al. 2012).

In brief, we assume that there are no color gradients in galaxies between the K_s band and the IRAC and MIPS bands. The K_s band is then used as a high-resolution template image to deblend the IRAC and MIPS photometry. Each source extracted from the K_s image is convolved with a kernel derived from bright PSF stars in the K_s and IRAC/MIPS images. The convolved galaxies are then fit as templates in the IRAC and MIPS bands with the total flux left as a free parameter. In this process, all objects in the image are fit simultaneously. Once the template fitting is converged, a "cleaned" image is produced for each object in the catalog by subtracting off all nearby sources (for an example of this process see Figure 1 of Wuyts et al. 2007). Aperture photometry is then performed on the cleaned image of each source. For the IRAC (MIPS) channels the photometry is performed in a 3″ (5″) diameter aperture for each object. This flux is then corrected to a flux within the 2.″1 color aperture via

$$F_{\mathrm{IRAC}}(2.''1) = F_{\mathrm{IRAC,cleaned}}(3'') \times \frac{K_{\mathrm{conv,worst\text{-}PSF}}(2.''1)}{K_{\mathrm{conv,IRAC}}(3'')}, \quad (3)$$

where $K_{\mathrm{conv,worst\text{-}PSF}}(2.''1)$ is the flux in the PSF-matched K_s image in the color aperture and $K_{\mathrm{conv,IRAC}}(3'')$ is the flux in the K_s image convolved to the IRAC PSF. Given that MIPS fluxes are primarily used to indicate star formation rates (SFRs), and are not used for colors, within the catalog the MIPS fluxes are listed as total fluxes rather than color fluxes. The MIPS fluxes have been converted to total fluxes using an aperture correction of a factor of 3.7, as listed in the MIPS instrument handbook.[8]

3.6. GALEX Photometry

The image quality of the *GALEX* NUV and FUV data are also substantially poorer than that available from the ground-based data (∼4″–5″). We cleaned and photometered the *GALEX* data using the same source-fitting code as for the IRAC and MIPS data. For the *GALEX* data we use the CFHT u^*-band data as a template rather than the K_s-band because the u^* band and the FUV and NUV bands have a close correspondence in wavelength. This required creating a new source list based on the u^* images and then matching that source list to the K_s source list. When performing this matching we use a conservative matching tolerance (<0.″5) to ensure only true counterparts are matched

[8] http://irsa.ipac.caltech.edu/data/SPITZER/docs/mips/mipsinstrumenthandbook

to the K_s-selected catalog. No *GALEX* photometry is provided for K_s-selected sources that do not have a clear match to the u^*-selected sources. We note that only the *GALEX* photometry is provided by matching sources, the u^*-band photometry itself is still measured using the standard PSF matching method and SExtractor in dual-image mode.

3.7. zCOSMOS Spectroscopic Redshifts

We match the photometric catalog to the catalog of spectroscopic redshifts ($z_{\rm spec}$) available from the zCOSMOS 10k bright sample (Lilly et al. 2009). That catalog contains ∼10,000 redshifts for galaxies with $i' < 22.5$. Due to the bright limit, the majority of redshifts in the catalog are at $0.1 < z < 1.5$. The matching is performed for the subset of zCOSMOS sources with redshift confidence classes in the range $3 < {\rm CC} < 5$. These are the highest-confidence spectroscopic redshifts, and should be 99% accurate (Lilly et al. 2007). We match only the high-confidence $z_{\rm spec}$ because these are used to determine offsets in the zero points in various filters (Section 4.1), and to determine quantities such as stellar masses and rest-frame colors. Uncertain $z_{\rm spec}$ can be extremely wrong resulting in unphysical results for this process.

Matching is done using an 0.″5 search radius. The optical i^+-band and the UltraVISTA K_s-band are well-registered so unique matches are found for all sources. Overall, there are 5105 $z_{\rm spec}$ from zCOSMOS matched to sources in the K_s-selected catalog.

3.8. Corrections for Bright Stars and Bad Regions

The COSMOS field is large enough that it contains regions with very bright stars. These bright stars create reflections and large diffraction spikes that make the photometry for galaxies in those regions unreliable. In the catalog we provide a parameter, `contamination`, which indicates whether an object's photometry has been contaminated by a nearby bright star. The contamination is determined by first generating a source list of optically bright stars within the COSMOS field from the USNO-B catalog, as well as a list of NIR-bright stars from the 2MASS catalog (Skrutskie et al. 2006). We determined an empirical relation between the brightness of the star and radius of the contaminated photometry. All objects that are within the contamination radius of a bright star in either the optical or NIR are then given a contamination flag = 1.

In general we have been conservative with the contamination radius in order to provide the most reliable photometric catalogs possible. Still, the total area considered to be contaminated by bright stars is fairly modest. The full coverage region of the catalog covers an area of 1.68 deg^2, whereas the usable, uncontaminated region covers 1.62 deg^2. This means only ∼4% of the total area is lost to bright stars.

The Subaru optical bands also contain some small square-like regions throughout the survey that do not have data. Some of these regions are located at the central few pixels of bright stars, but others occur throughout the survey area, seemingly at random locations. It is unknown what the source of these regions are, but they occur most frequently in the i^+ band data. The pixel values in these regions have either been set to "nan" or 10^{-31}, and failure to mask these regions causes nonsensical fluxes to be measured for nearby galaxies. The regions occur frequently enough that we developed a procedure for identifying them.

A pixel map of each optical band showing the location of the "nan" region is made. This map is then smoothed with a kernel that grows the size of the contaminated regions by a factor of ∼2. When the final catalog is constructed these mask regions are then checked for each object, in each filter. If the object lies within a contaminated region for that filter, the flux in that filter is set to −99, and the parameter `nan_contam` is incremented by 1. This setting for the flux makes the photometric redshift fitting code (Section 4) and stellar population fitting code (Section 5) effectively consider the object not observed in that particular filter. This is useful because the nan regions are in different locations in various filters. The filter-by-filter masking allows us to effectively keep objects with some contamination in the catalog, but remove only the photometry in the contaminated filters. Because `nan_contam` is incremented, it is a metric of the number of filters that have contamination for a given object. It is recommended to only use objects with contamination in <5 filters.

3.9. Photometric Catalog Layout and Usage

The layout of the full photometric catalog is summarized in Table 2. The catalog is presented as a set of fluxes in the 2.″1 color aperture with an AB zero point of 25.0. These can be converted to AB magnitudes via $m_x = -2.5\log_{10}(f_x) + 25.0$, where x denotes a given filter. Also given is the total K_s-band magnitude from SExtractor's `flux_auto`, which has been corrected to a total flux using the growth curve of the PSF stars. The flux in any filter can be converted to a total flux via

$$f_{x,\rm tot} = f_x \times \frac{f_{Ks,\rm tot}}{f_{Ks}}. \quad (4)$$

The catalog contains the `star` indicator (= 1 for stars, = 0 for galaxies), as well as the `contamination` and `nan_contam` parameters described in Section 3.8. Lastly, we include a parameter `USE`. Selecting objects with `USE` = 1 in the catalog selects the subset of objects with `star` = 0, `contamination` = 0, `nan_contam` < 5, and $K_s < 23.9$. The latter is the 5σ depth of the survey in the color aperture. Objects with `USE` = 1 are considered to be galaxies with uncontaminated photometry with fluxes sufficiently bright that the photometry is still accurate.

4. PHOTOMETRIC REDSHIFTS

Photometric redshifts ($z_{\rm phot}$) are calculated for all galaxies using the EAZY software (Brammer et al. 2008). EAZY determines the $z_{\rm phot}$ for galaxies by fitting their spectral energy distributions (SEDs) to linear combinations of seven templates, six of which are derived from the PEGASE models (Fioc & Rocca-Volmerange 1999), as well as an additional red template from the models of Maraston (2005). A detailed description of EAZY's fitting process can be found in Brammer et al. (2008). EAZY also accounts for potential mismatches between the data and the templates via the "template error function" (see Brammer et al. 2008). The template error function weights photometric points in the template fitting based on their implied rest-frame wavelength. In particular, when using the default template error function, measurements corresponding to the rest-frame NIR are down-weighted compared to the rest-frame optical given the current uncertainties in models at these wavelengths (e.g., Maraston 2005; Kriek et al. 2010).

Photometric redshifts were determined with EAZY primarily using the default set of parameters, although several optimizations were added after examination of the initial output. For the first run we used the seven default templates, the v1.0 template error function, the $K_{s,\rm tot}$ magnitude prior, and allowed photometric redshift solutions in the range $0 < z < 6$.

Table 2
Summary of Photometric Catalog

Column	Parameter Name	Description
1	id	Object identifier number
2, 3	ra, dec	Right ascension and declination in J2000 decimal degrees
3, 4	xpix, ypix	Pixel position of object in the K_s image
5	Ks_tot	Total K_s-band flux with additional aperture correction applied
6	eKs_tot	Error in total K_s-band magnitude determined from scaled empty apertures
7–67	X, eX	Flux and error in filter X measured in a 2.″1 aperture from PSF-matched images
68	K_flag	SExtractor's FLAG output for the K_s-band image
69	K_star	SExtractor's CLASS_STAR output from the K_s band image
70	K_Kron	Kron radius in the K_s-band
71	apcor	Aperture correction that has been applied to FLUX_AUTO to determine Ks_tot
72, 73, 74	z_spec, z_spec_cc, z_spec_id	zCOSMOS spectroscopic redshift, spectroscopic redshift quality flag, and ID number
75	star	Star/galaxy indicator determined from color–color plot (star = 1, galaxy = 0)
76	contamination	Indicates proximity to a bright star (contaminated = 1, uncontaminated = 0)
77	nan_contam	Number of filters where object lies near gaps in photometry or near a saturated star
78, 79	orig_cat_id, orig_cat_field	ID and tile of object in the tile catalog
80	USE	Indicates galaxies with uncontaminated photometry and S/N > 5

Comparison of the resulting $z_{\rm photo}$ with the $z_{\rm spec}$'s from zCOSMOS was good, although there were some significant outliers (∼5%). Some experimentation showed that catastrophic outliers could largely be eliminated by running EAZY with a 5% systematic error included for all photometric bands. The 5% systematic helps reduce catastrophic outliers because the optical medium bands have narrow bandpasses and therefore problems in the photometry in consecutive bands can create very sharp features in the SED.

After eye-examination of the best-fit models for a subsample of the galaxies it became apparent that there were two populations of galaxies that were not well-described with the default template set. The first of these were galaxies at $z > 1$ with post-starburst-like SEDs. These galaxies tend to have strong Balmer breaks, but also a continuum that is very blue redward of the Balmer break, and it is not possible to reproduce such an SED with the default EAZY template set. We added a one-gigayear-old single-burst Bruzual & Charlot (2003) model to the template set and this significantly improved the fits for these galaxies. The need for a similar template in EAZY was also reported by Onodera et al. (2012).

The second set of galaxies with problematic fits was a population of UV-bright galaxies at $1.5 < z < 3.5$ with UV continua that were blue, but still redder than could be produced with the default templates. Given that the catalog is K_s-selected, these are likely to be the most massive part of the Lyman break galaxy (LBG) population, and they may have slightly more dust extinction than lower-mass LBGs. We added a slightly dust-reddened young population to the template set and this improved the fit to this population.

4.1. Zero-point Offsets

Photometric redshifts are extremely sensitive to errors in photometric zero points. This is especially pronounced when medium bandwidth filters are used as they tend to be closely spaced in wavelength and errant zero points can create sharp features in the SEDs. A common procedure to ensure the best-quality $z_{\rm photo}$ is to refine the photometric zero points of a catalog using a subsample of galaxies with spectroscopic redshifts (e.g., Ilbert et al. 2006, 2009; Brammer et al. 2011; Whitaker et al. 2011).

We perform this process using an iterative zero-point offset code developed for the NMBS (see Whitaker et al. 2011). We use only the highest-quality spectroscopic redshifts from zCOSMOS ($3 < \rm CC < 5$) as well as a set of 19 $z_{\rm spec}$ of massive galaxies at $z > 1$ from other programs in the COSMOS field (Onodera et al. 2012; van de Sande et al. 2011, 2013; Bezanson et al. 2013).

The procedure is as follows. First, EAZY is run on SEDs of the spectroscopic redshift sample fixing the photometric redshift to the spectroscopic redshift. The median offset in each filter compared to the best-fit template is measured for the full sample. The photometry for all galaxies is adjusted by this amount and EAZY is re-run. The process is repeated until the median offsets converge to a value of less than 0.01 mag in every filter. When calculating the offsets, the K_s-band is used as the "anchor" filter and is not adjusted. Given that the offsetting is based on colors, having a filter that is not adjusted is important so that the zero points do not drift in an absolute sense while the relative zero points are being improved. We note though that the K_s zero point was initially adjusted by 0.08 mag to bring it into better agreement with other surveys (see the Appendix). We have also not computed offsets for the IRAC and *GALEX* bands. It is unclear how well the EAZY templates should reproduce these wavelength ranges and so we chose to not iterate them as it may introduce incorrect colors because of the adopted template set.

In Table 3 we list the zero-point offsets determined for all bands. These are typically small for the optical broad-band filters (∼0.05 mag), but can be larger for the optical medium bands (up to 0.17 mag). Similar size offsets for those bands were also found in the NMBS (see Table 4 in Whitaker et al. 2011). Offsets of the order of 0.1–0.2 mag are seen for the UltraVISTA bands. These are comparable to the offsets seen between the UltraVISTA data and the CFHT WIRCAM data by McCracken et al. (2012).

4.2. Photometric Redshift Catalog and Comparison with Spectroscopic Redshifts

In Table 4 we show the layout of the photometric redshift catalog from EAZY. The parameter $z_{\rm peak}$ corresponds to the peak probability of the $P(z)$ function, and is considered to be the most likely $z_{\rm phot}$. The 68% and 95% confidence intervals are calculated by integrating the $P(z)$ function.

In the left panel of Figure 5 we show a comparison between the $z_{\rm phot}$ and $z_{\rm spec}$ for the zCOSMOS redshifts, as well as the high-redshift spectroscopic samples from Onodera et al. (2012),

Table 3
Zero-point Offsets Determined from Spectroscopic Redshifts

Filter	Offset (Mag)
FUV	...
NUV	...
u^*	−0.10
B_j	−0.12
g^+	−0.11
V_j	0.03
r^+	−0.06
i^+	−0.03
z^+	−0.06
IA427	−0.12
IA464	−0.12
IA484	−0.08
IA505	−0.07
IA527	−0.09
IA574	−0.17
IA624	−0.09
IA679	0.06
IA709	−0.10
IA738	−0.15
IA767	−0.13
IA827	−0.17
Y	−0.10
J	−0.14
H	−0.18
K_s	−0.08[a]
3.6 μm	...
4.5 μm	...
5.8 μm	...
8.0 μm	...
24 μm	...

Notes. Offsets are defined such that $ZP_{EAZY} = ZP_{nominal}$ + offset.
[a] The K_s zero-point offset is determined by comparing photometry with other surveys, not from the spectroscopic redshifts.

Bezanson et al. (2013), and van de Sande et al. (2013). In general, the photometric redshifts compare well to the spectroscopic redshifts, although we note that this comparison is primarily from galaxies at $z_{spec} < 1.5$. Galaxies that are $>3\sigma$ outliers from the one-to-one relation based on their redshift errors from EAZY are considered as catastrophic outliers. The fraction of these galaxies is low (1.56%), and the rms dispersion around the one-to-one relation for the remainder of the sample is 0.013 in $\delta z/(1+z)$.

The z_{phot} accuracy compares well to the z_{phot} accuracy for other catalogs in the COSMOS field. Ilbert et al. (2009) measure a catastrophic outlier fraction of 0.7%, and $\delta z/(1+z) = 0.007$. This is slightly better than for our K_s-selected catalog; however, Ilbert et al. (2009) use a more restricted set of z_{spec} for this test (∼4000 z_{spec} compared to ∼5000 z_{spec} in our catalog). Whitaker et al. (2011) find a catastrophic outlier fraction of 5% with a $\delta z/(1+z) = 0.008$. This is a higher outlier fraction but a better rms dispersion. This difference is mostly likely from our inclusion of a 5% systematic error in the error bars when fitting with EAZY which reduces catastrophic outliers at the expense of some redshift precision.

4.3. Comparison with NMBS Photometric Redshifts

The zCOSMOS z_{spec} provide a useful diagnostic of the accuracy of the z_{phot}; however, there are few z_{spec} at $z > 1.5$, leaving the accuracy in this redshift range less certain. The NMBS covers 0.22 deg^2 of the COSMOS field and here we compare the z_{phot} determined between each survey. The NMBS catalog has data similar to those in the UltraVISTA catalog. It is also a K_s-selected catalog and contains photometry from the Subaru broad-band and medium-band data. It also uses the same source-fitting code for the *GALEX* and IRAC photometry and the z_{phot} for the NMBS have been computed using EAZY. The primary differences are that the NMBS has six NIR filters compared to four from UltraVISTA. This NMBS is also ∼0.6 mag shallower than UltraVISTA. The NMBS does have deeper optical photometry in the $u^*g'r'i'z'$ bands from the CFHTLS data which are not included in the UltraVISTA catalog.

In the left panel of Figure 6 we plot the $z_{phot,UVISTA}$ versus $z_{phot,NMBS}$. Dark circles are for galaxies that are above the 95% mass-completeness limit of the survey at a given redshift (see Muzzin et al. 2013), and light symbols are for those below the 95% mass-completeness limit. For the mass-complete sample, the agreement between UltraVISTA and NMBS is excellent. The fraction of galaxies at $0 < z < 4$ that are $>5\sigma$ outliers is 2.0%, with a scatter in $\delta z/(1+z) = 0.026$. Including the full sample of galaxies the number of $>5\sigma$ outliers increases to 3.7%.

In the right panel of Figure 6 we plot the difference between the z_{phot} as a function of the $z_{photo,NMBS}$. At $z > 1$, there is a slight systematic bias between the two surveys of $\delta z/(1+z) = 0.005$, with the z_{phot} from NMBS being slightly higher for a given galaxy. This was also suggested by the small number of galaxies in this redshift range with spectroscopic redshifts (Section 4.2). Small systematics like this are not completely unexpected. The NMBS used NIR medium bands in order to better trace the Balmer/4000 Å break and provide improved z_{photo} for galaxies at $z > 1.5$ (see Whitaker et al. 2011). Even with the slightly deeper data available from UltraVISTA, it would be unrealistic to expect NIR broad bands to perform as well as NIR medium bands when determining z_{phot}.

Table 4
Summary of Photometric Redshift Catalog

Column	Parameter Name	Description
1	id	Object identifier number
2	z_{spec}	Spectroscopic redshift from zCOSMOS (no redshift = −1)
3	chi	χ^2 of the best-fitting template
4	z_{peak}	Photometric redshift from the peak of the $P(z)$ distribution
5, 6	l68, u68	Upper and lower 68% confidence intervals on z_{peak}
7, 8	l95, u95	Upper and lower 95% confidence intervals on z_{peak}
9, 10	l99, u99	Upper and lower 99% confidence intervals on z_{peak}
11	$peak_{prob}$	Peak probability
12	nfit	Number of filters used to determine z_{peak}

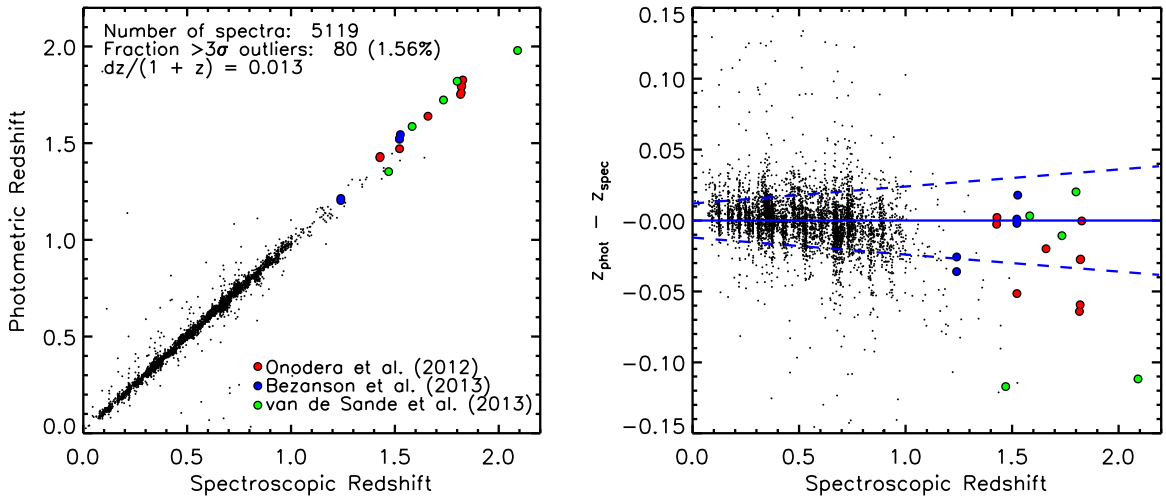

Figure 5. Left panel: photometric redshift from the UltraVISTA K_s-selected catalog vs. spectroscopic redshift from the zCOSMOS catalog (black dots). Only galaxies with high-quality spectroscopic redshifts and uncontaminated photometry are shown. Red galaxies with high-quality spectroscopic redshifts from Onodera et al. (2012) are plotted as red symbols. Also plotted are red galaxies with redshifts from Bezanson et al. (2013) and van de Sande et al. (2013). Right panel: difference between spectroscopic redshift and photometric redshift as a function of spectroscopic redshift. The dashed lines show the rms dispersion of $\delta z = 0.13/(1+z)$, which is calculated from the zCOSMOS sample once catastrophic outliers are removed. The Onodera et al., Bezanson et al., and van de Sande et al. spectroscopic redshifts suggest that the rms dispersion at $z > 1.4$ is likely to be larger than that measured from the zCOSMOS sample.

(A color version of this figure is available in the online journal.)

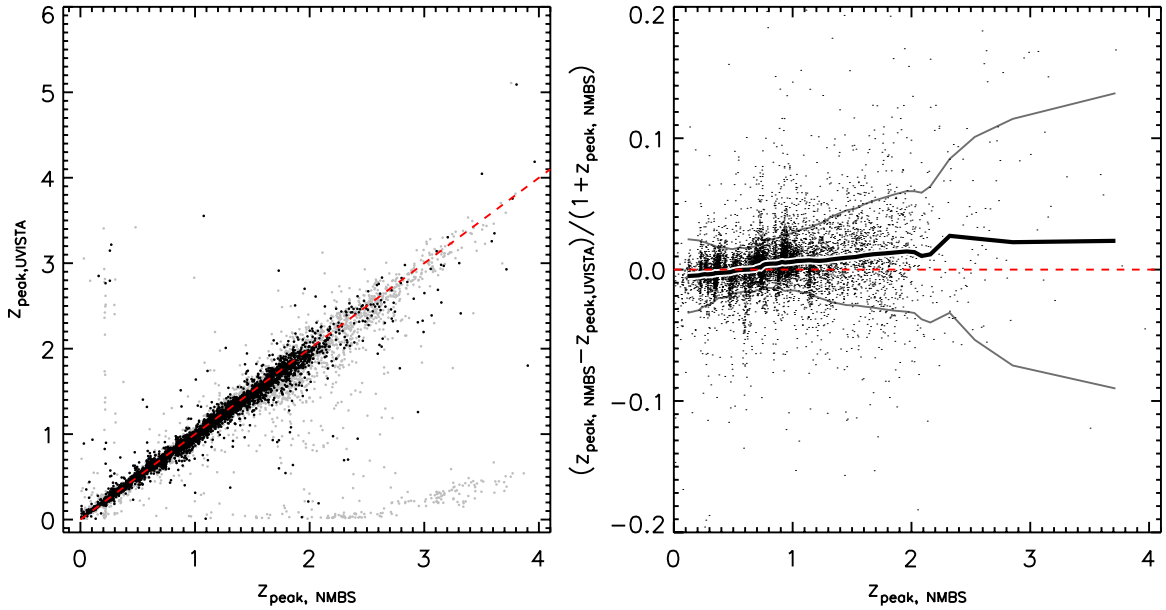

Figure 6. Left panel: photometric redshifts from UltraVISTA vs. photometric redshifts from the NMBS in the overlap region between the two surveys. Galaxies with stellar masses >95% mass-completeness limit for the survey are shown as dark circles, and those below the limit are shown as light circles. Right panel: difference in photometric redshift between UltraVISTA and NMBS as a function of photometric redshift. The solid curve shows the median difference and the gray curves show the rms. The agreement between the two surveys is extremely good, particularly for the mass-complete sample where the $>5\sigma$ outlier fraction is 2.0% and the rms is $\delta z/(1+z) = 0.026$.

(A color version of this figure is available in the online journal.)

4.4. Correction for Extreme Blue Galaxies

In the left panel of Figure 6, it is clear that a subsample of the fainter galaxies have $z_{\rm phot}$ that do not agree well between the surveys. These are seen as the line of galaxies that have $z_{\rm phot} < 0.5$ in UltraVISTA but a range of much higher $z_{\rm phot}$ in NMBS. There is a complementary population running along the Y-axis; however, it is substantially smaller suggesting that on average the $z_{\rm phot}$ of this population may have been underestimated in the UltraVISTA catalog.

As an example, we show the SEDs and $P(z)$ of one of these objects in both surveys in Figure 7. Examination of the $P(z)$ for these galaxies in both surveys shows that they are frequently bi-modal with a peak both at $z < 0.5$, as well as a peak at $z > 1.5$. The SEDs of these galaxies are also typically very blue. They have a single feature, which is a break starting in the bluest optical bands. This break is interpreted as the Balmer-break in the low-redshift solution, and as the Lyman break for the high-redshift solution.

These galaxies are problematic, but very few of them have spectroscopic redshifts so determining which solution is the correct one is non-trivial. Several lines of evidence point to the NMBS solution of high-redshift Lyman breaks being the correct ones. Firstly, many of the galaxies with the high-redshift

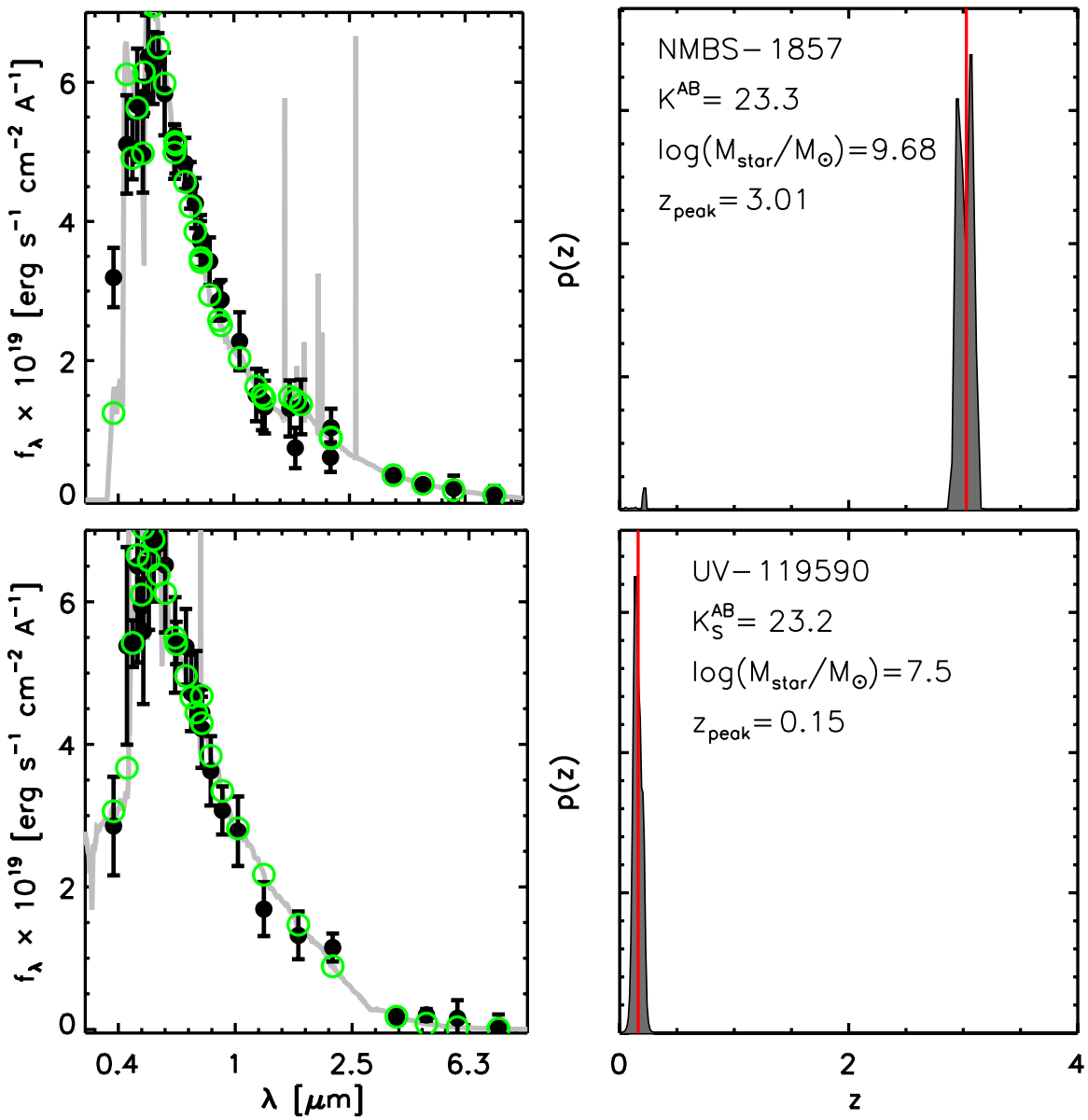

Figure 7. Example of an extreme blue galaxy with a photometric redshift that is very different between the UltraVISTA and NMBS. The NIR medium bands in NMBS suggest a Balmer break, which is less well-resolved with the UltraVISTA broad bands. We have corrected the photometric redshift of the extreme blue galaxies at $z < 0.5$ to their best fit solution at $z > 1.5$. The correction is primarily aesthetic, as these galaxies make up <1% of all galaxies and are typically well below the mass-completeness limit of the survey (at either redshift).

(A color version of this figure is available in the online journal.)

solution do show weak Balmer breaks in the NIR medium bands (see Figure 7). These breaks are well traced by the NIR medium bands. They are also seen in the UltraVISTA broad bands, but are not as well traced, given that there are less filters. As in Figure 7, the break in UltraVISTA is usually manifest as a single deviant point (either the Y or J band) to an otherwise good fit. Secondly, the NMBS uses the deep CFHTLS u^* data which covers only a portion of the UltraVISTA field. It also uses as smaller color aperture (1.″5 compared to 2.″1), so the photometric errors in the u^* band in the NMBS are smaller by a factor of ∼1.5. This makes the u^* band breaks clearer, and in many cases rules out the possibility of the break being the Balmer break, which is a weaker feature. Lastly, once rest-frame colors are computed (see Section 5.2), it is clear that many of these galaxies lie in a portion of the UVJ diagram not populated by other galaxies.

Given these lines of evidence, it is reasonable to expect that most of these galaxies are likely to be high-redshift galaxies and so we apply a correction to their photometric redshift. The NMBS only covers a fraction of the UltraVISTA field, so we cannot use those data to improve things. Instead, we identify the population based on their location in the UVJ diagram. Galaxies that are much bluer than the overall $z < 0.5$ population in both $U - V$ and $V - J$ (rest-frame) are selected as the candidate high-z population. For these galaxies we re-run EAZY, but only allowing solutions in the range $1.5 < z < 6.0$. This prevents a solution at $z < 0.5$ and forces the $z_{\rm phot}$ to the $z > 1.5$ solution.

While this correction is somewhat ad hoc we note that it affects only a small fraction of galaxies in the catalog. Of the total sample of 262,615 sources, only 2415 (<1%) are affected by this correction. More importantly, of this 1%, the majority are quite faint, and as shown in Figure 6, almost none lie above

Table 5
Summary of Stellar Population Parameter Catalog

Column	Parameter Name	Description
1	id	Object identifier number
2, 3, 4	z, l68_z, u68_z	Photometric redshift and 68% confidence intervals from EAZY
5, 6, 7	ltau, l68_ltau, u68_ltau	Best-fit value of log(τ) and 68% confidence intervals
8, 9, 10	lage, l68_lage, u68_lage	Best-fit value of log(t) and 68% confidence intervals
11, 12, 13	A_v, l68_A_v, u68_A_v	Best-fit value of A_v and 68% confidence intervals
14, 15, 16	lmass, l68_lmass, u68_lmass	Best-fit value of log($M_{\rm star}/M_{\odot}$) and 68% confidence intervals
17, 18, 19	lsfr, l68_lsfr, u68_lsfr	Best-fit value of log(sfr) from the SED and 68% confidence intervals
20, 21, 22	lssfr, l68_lssfr, u68_lssfr	Best-fit value of log(ssfr) from the SED and 68% confidence intervals
23	chi	χ^2 of best-fitting model

the mass-completeness limit of the survey regardless of whether their solution is at high redshift or low redshift. Because of this, the correction of their $z_{\rm phot}$ does not affect any results based on the mass-complete sample.

5. SED MODELING AND STELLAR POPULATION PARAMETERS

5.1. Stellar Masses, Ages, and Dust Extinction

Stellar population parameters are determined by fitting galaxy SEDs using the FAST code (Kriek et al. 2009). We provide two catalogs of population parameters for the catalogs: one fit to SEDs generated using the Bruzual & Charlot (2003) models and one fit to SEDs generated using the Maraston (2005) models. For both sets of models we assume solar metallicity, a Chabrier (2003) initial mass function (IMF), and a Calzetti et al. (2000) dust extinction law.

To construct the set of template SEDs, we assume galaxies have exponentially declining star formation histories (SFHs) of the form SFR $\propto \exp(-t/\tau)$, where t is the time since the onset of star formation and τ is the e-folding star formation timescale in units of Gyr. We allow Log(τ) to vary between 7.0 and 10.0 in increments of 0.2, and Log(t) to vary between 7.0 and 10.1 in increments of 0.1. For all galaxies we restrict t to be less than the age of the universe at the redshift of the galaxy. We also fit for visual attenuation of the galaxies (A_v) assuming a uniform dust screen geometry and allow A_v to vary between 0 and 4. All galaxies are fit assuming their redshift is the best-fit EAZY $z_{\rm phot}$. In all, we fit four parameters per galaxy: τ, t, A_v, and a normalization. The stellar mass ($M_{\rm star}$) is then determined from mass-to-light ratio of the best-fit SED multiplied by the best-fit normalization of the SED. The layout of the catalogs of best-fit stellar population parameters is summarized in Table 5.

In Figure 8 we show a comparison between the $M_{\rm star}$ measured for the galaxies in the NMBS catalog versus the $M_{\rm star}$ measured for galaxies in the UltraVISTA catalog as a function of mass. In general the agreement is good. There is a systematic difference of 0.05 dex between the two with galaxies being more massive in the NMBS catalog.

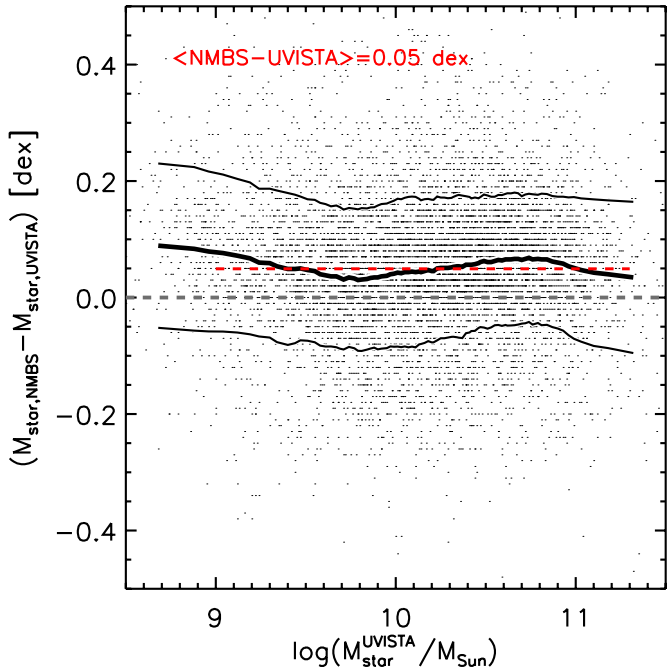

Figure 8. Comparison of stellar masses determined in the NMBS and UltraVISTA as a function of stellar mass. The dark solid curve is the running median and the lighter solid curves encompass the 68 percentile of the distribution. There is a trend for systematically higher masses in the NMBS, but no significant trend with stellar mass.

(A color version of this figure is available in the online journal.)

5.2. Rest-frame Colors

The rest-frame $U - V$ versus $V - J$ diagram has become a popular way to differentiate between star-forming and quiescent galaxies (Labbé et al. 2005; Wuyts et al. 2007; Williams et al. 2009; Brammer et al. 2011; Whitaker et al. 2011; Patel et al. 2012, 2013). This approach is similar to the observed BzK diagram that has been used in the past (e.g., Daddi et al. 2005, 2007, and numerous others), but allows for a cleaner separation of star-forming and quiescent galaxies because colors are defined in the rest-frame rather than the observed frame, removing any redshift-dependence of the colors.

We calculate rest-frame $U - V$ and $V - J$ colors for all galaxies using EAZY. EAZY determines the colors by integrating the best-fit SED through the redshifted filter curves over the appropriate wavelength range. For the U and V filter we use the response curves defined in Maíz Apellániz (2006), and for the J filter we used the 2MASS filter curve from Skrutskie et al. (2006). The rest-frame $U - V$ and $V - J$ colors are listed in Table 6.

5.3. The UVJ Diagram

In Figure 9 we plot grayscale histograms of the $U - V$ versus $V - J$ colors for galaxies with S/N(K_s) > 7 in various redshift bins between $0 < z < 3.5$. The galaxy population is clearly separated into two clumps in color–color space up to $z = 2$. The reddest of the two clumps has colors similar to that of quiescent and passively evolving galaxies, whereas the bluer clump has a much wider range of colors, usually interpreted

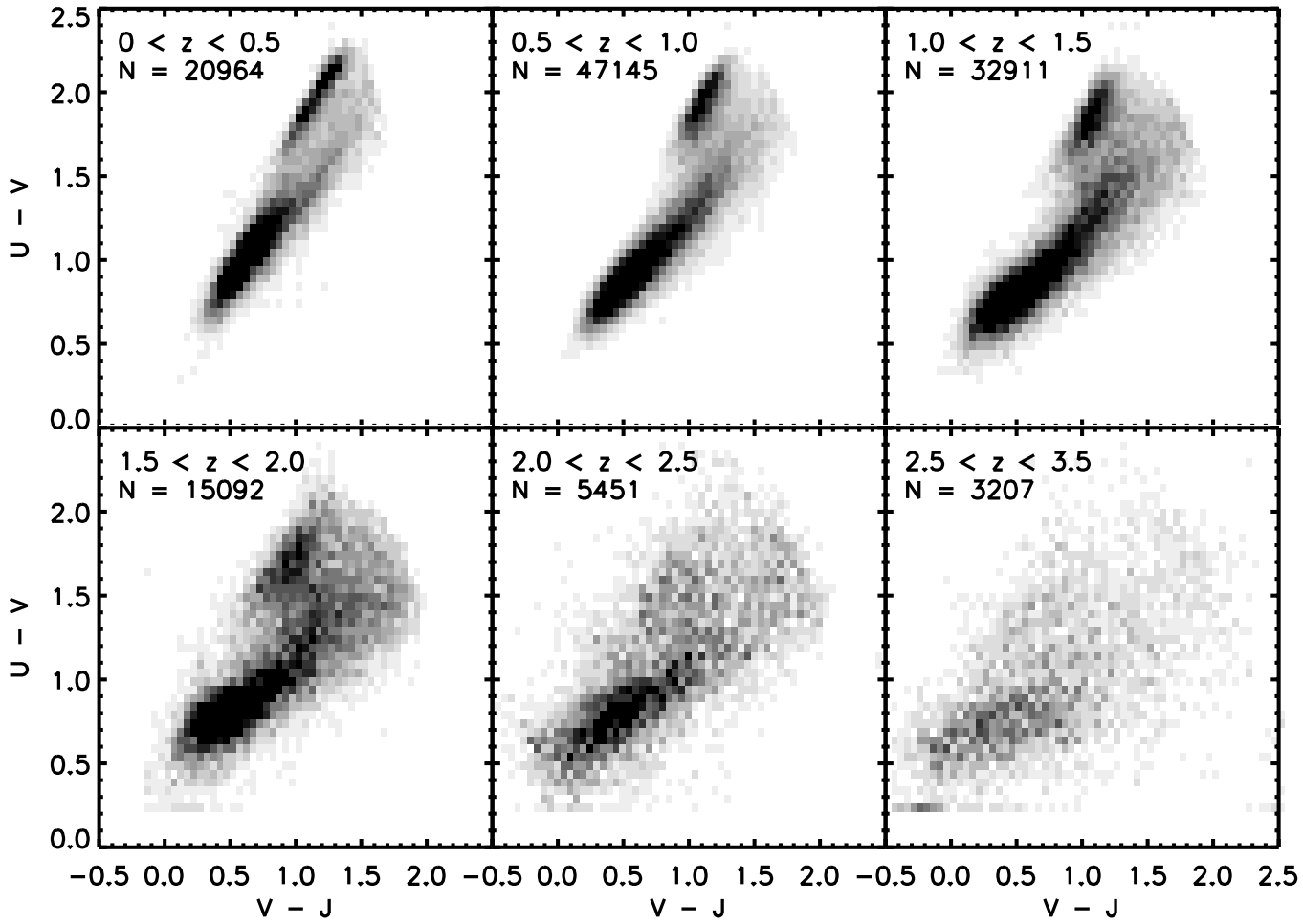

Figure 9. The $U - V$ vs. $V - J$ color–color diagram for galaxies with S/N(K_s) > 7. The well-known bi-modality between quiescent galaxies and star-forming galaxies can be clearly seen in the galaxy population up to $z \sim 2$. Thereafter the bi-modality becomes less pronounced. Also visible in the figure is the continued reddening of the passive population with decreasing redshift. This reddening is expected from a passively evolving population.

Table 6
Summary of Rest-frame Color and UV and IR Luminosity Catalog

Column	Parameter Name	Description
1	id	Object identifier number
2	$U - V$	Rest-frame $U - V$ color
3	$V - J$	Rest-frame $V - J$ color
4, 5, 6	L_{2800}	Total UV luminosity and 68% confidence intervals
7, 8, 9	$L_{\rm IR}$	Total IR luminosity and 68% confidence intervals
10, 11, 12	$\rm SFR_{UV,uncorr}$	UV star formation rate and 68% confidence intervals, uncorrected for dust extinction
13, 14, 14	$\rm SFR_{IR}$	IR star formation rate and 68% confidence intervals

as the star-forming population with a range of dust extinctions and geometries (e.g., Labbé et al. 2005; Williams et al. 2009; Brammer et al. 2009; Patel et al. 2013). In general, the *UVJ* diagram in COSMOS shows the same structure as has been seen in other surveys (e.g., Williams et al. 2009; Whitaker et al. 2011); however, the superior volume in UltraVISTA provides an increase in the number of galaxies by a factor of ∼4–5.

An interesting feature of the diagram revealed by the large sample of galaxies in UltraVISTA is the continued reddening of the quiescent population with decreasing redshift. Whereas the quiescent population is primarily located in a single clump with colors of $U - V = 1.7$ and $V - J = 1.0$ at $z = 2$, it appears as more of a sequence at $z = 0$. This reddening with decreasing redshift is precisely what is expected for a passively evolving population of galaxies (e.g., Wuyts et al. 2007).

It is tempting to make further inferences on the evolution of the galaxy population using Figure 9. Doing so requires a more quantitative analysis; in particular, it is important to adopt the appropriate limits in $M_{\rm star}$ with redshift in order to define a mass-complete sample. Figure 9 is meant to be illustrative and is made with a S/N cut, not a $M_{\rm star}$-cut, so it becomes increasingly skewed to lower-mass galaxies at lower redshift. A full analysis of the *UVJ* diagram using the appropriate mass limits will be presented in a future paper.

5.4. Example SEDs

As an example of the quality of the SEDs and SED fitting, we show examples of the observed galaxy SEDs and the best-fit EAZY SEDs from the catalog in Figures 10–12. At each

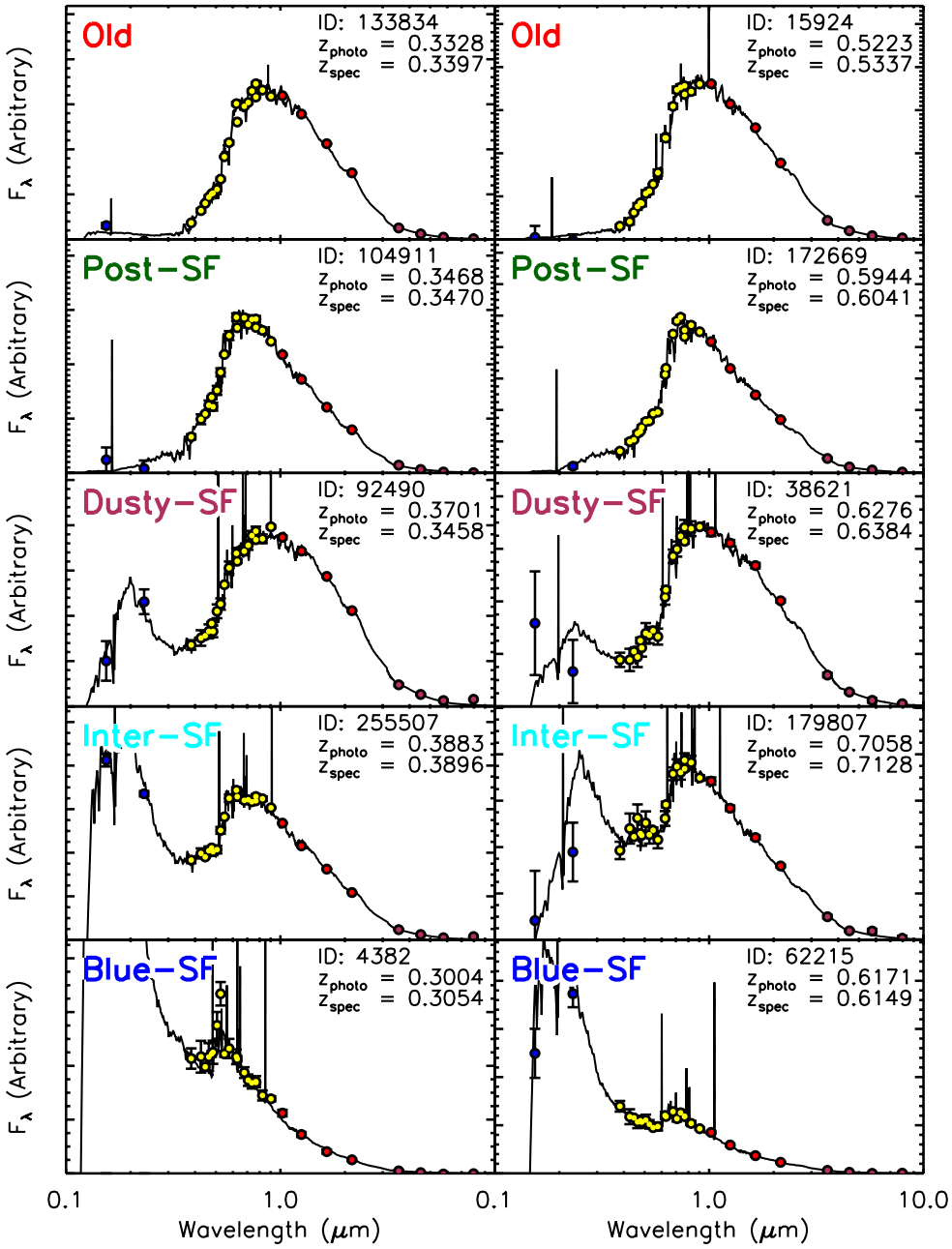

Figure 10. Example SEDs for galaxies of different types at $0 < z < 1.0$ with S/N(K_s) > 10 chosen from their location in the *UVJ* diagram (see text). In general the fits are very good, and clear features such as the Lyman break, Balmer break, and 4000 Å break can be seen in the galaxy populations.
(A color version of this figure is available in the online journal.)

redshift, SEDs classified by their location in the *UVJ* diagram are shown in order to demonstrate the SEDs for a range of different galaxy types. We chose a total of five different SED classifications—two types of SEDs in the quiescent population and three types in the star-forming population. Within the quiescent population we chose those that are located near the red tip in $U - V$ versus $V - J$ (labeled "old"), and those that are near the blue tip in $U - V$ versus $V - J$, but still have quiescent colors. These blue-tip galaxies have colors that are similar to recently quenched galaxies, or "post-star-formation galaxies" (e.g., Kriek et al. 2010; Whitaker et al. 2012a) and are labeled "post-SF."

For the star-forming population, we divided the sequence of galaxies going from blue $U - V$ and blue $V - J$ colors, to red $U - V$ and red $V - J$ colors into three bins. The three regions cover the bluest population, an intermediate population, and the reddest (dustiest) population (labeled blue-SF, inter-SF, and dusty-SF, respectively).

The galaxies in each bin are chosen to have S/N(K_s) > 10, but are otherwise selected at random so that they are representative of typical SEDs for that SED type and redshift range. The only exception to this is that for the lowest redshift bin we use only galaxies that have z_{spec} from zCOSMOS in order to show the agreement between photometric and spectroscopic SEDs.

Figures 10–12 demonstrate the excellent quality of the SEDs and SED fitting, all the way up to $z = 2.5$. They also show how at $z < 1$ the optical medium bands trace the Balmer and 4000 Å break extremely well, and why such good quality z_{phot} can be determined. At $z > 1.5$ the UltraVISTA bands trace the break. In particular, it can be seen how the *Y*-band data is extremely

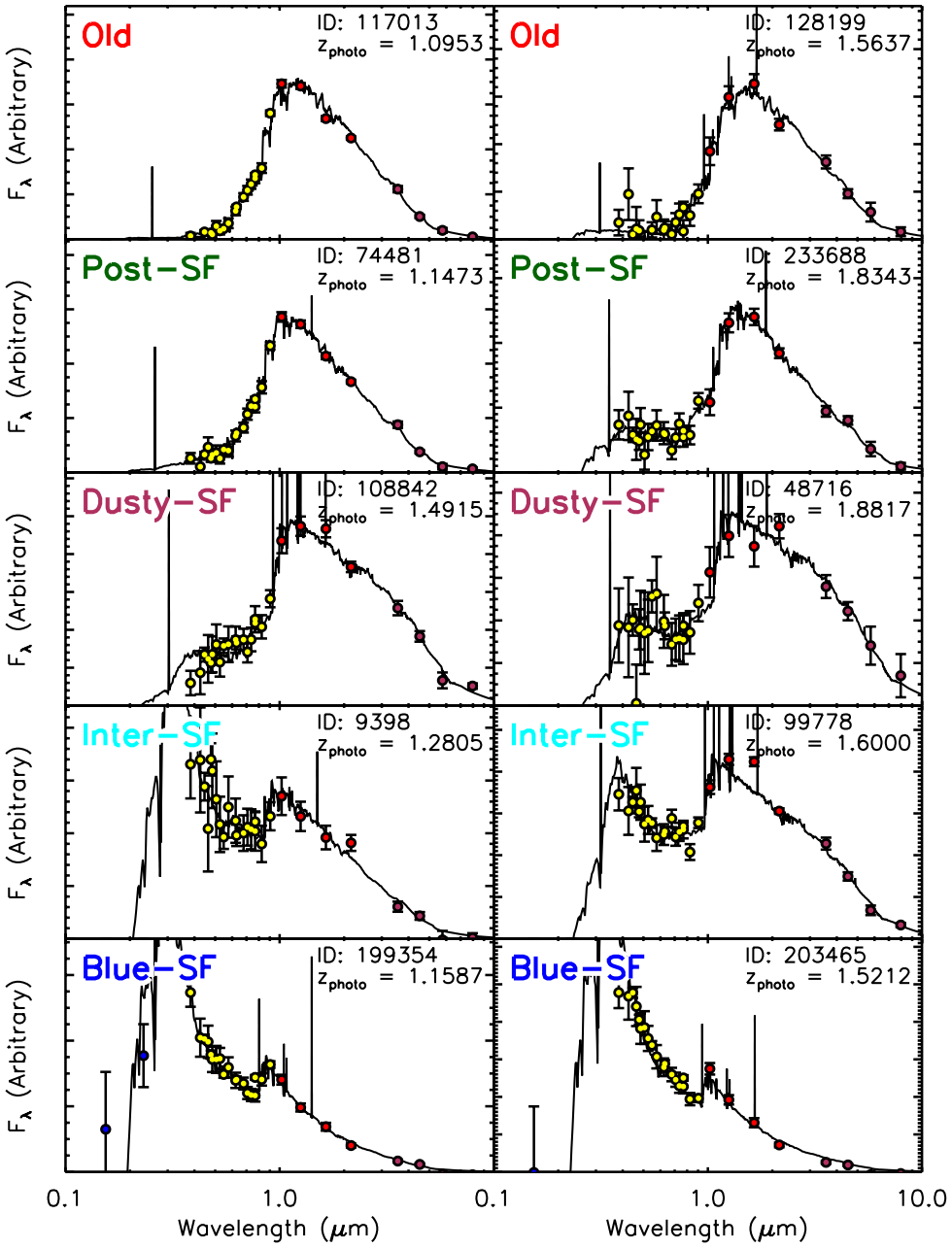

Figure 11. Same as Figure 10 but for galaxies at $1 < z < 2$.
(A color version of this figure is available in the online journal.)

useful for connecting what would be a large gap in wavelength space between the z'-band and J-band. At $z > 2.5$ the IRAC data become increasingly important because these are the only filters that remain redward of the break. The best-fit SEDs for all galaxies using EAZY and FAST for both BC03 and M05 models are available for download with the catalog.

5.5. UV and Infrared Luminosities and SFRs

The SED fitting to the BC03 and M05 models results in an estimated SFR for each galaxy (see Table 5). Those values can be considered total, dust-corrected SFRs (primarily constrained by the UV flux). They may be indicative; however, we caution against using those values in a quantitative way. This is because the estimated SFR is strongly influenced by the assumption of an exponentially declining SFH. If this is not the correct SFH (which is likely to be true for many star-forming galaxies, e.g., Maraston et al. 2010; Papovich et al. 2011), then they can be substantially in error.

A better measure of the instantaneous SFR comes from the rest-frame UV flux (L_{2800}) and the rest-frame total infrared luminosity ($L_{\rm IR}$). With the availability of rest-frame UV information (from *GALEX* to optical) as well as rest-frame MIR data (from MIPS-24 μm) we can calculate these quantities or the upper limits on them for all galaxies. These can then be converted to SFRs based on the standard conversion factors (e.g., Kennicutt 1998).

To determine L_{2800} we use EAZY. Similar to the rest-frame colors (Section 5.2), EAZY integrates the best-fit template over the wavelength range 2600–2950 Å to determine an L_{2800} for all galaxies. Because there are *GALEX* data, this quantity is constrained by data over the full redshift range of the galaxy population. The L_{2800} values are listed in Table 6.

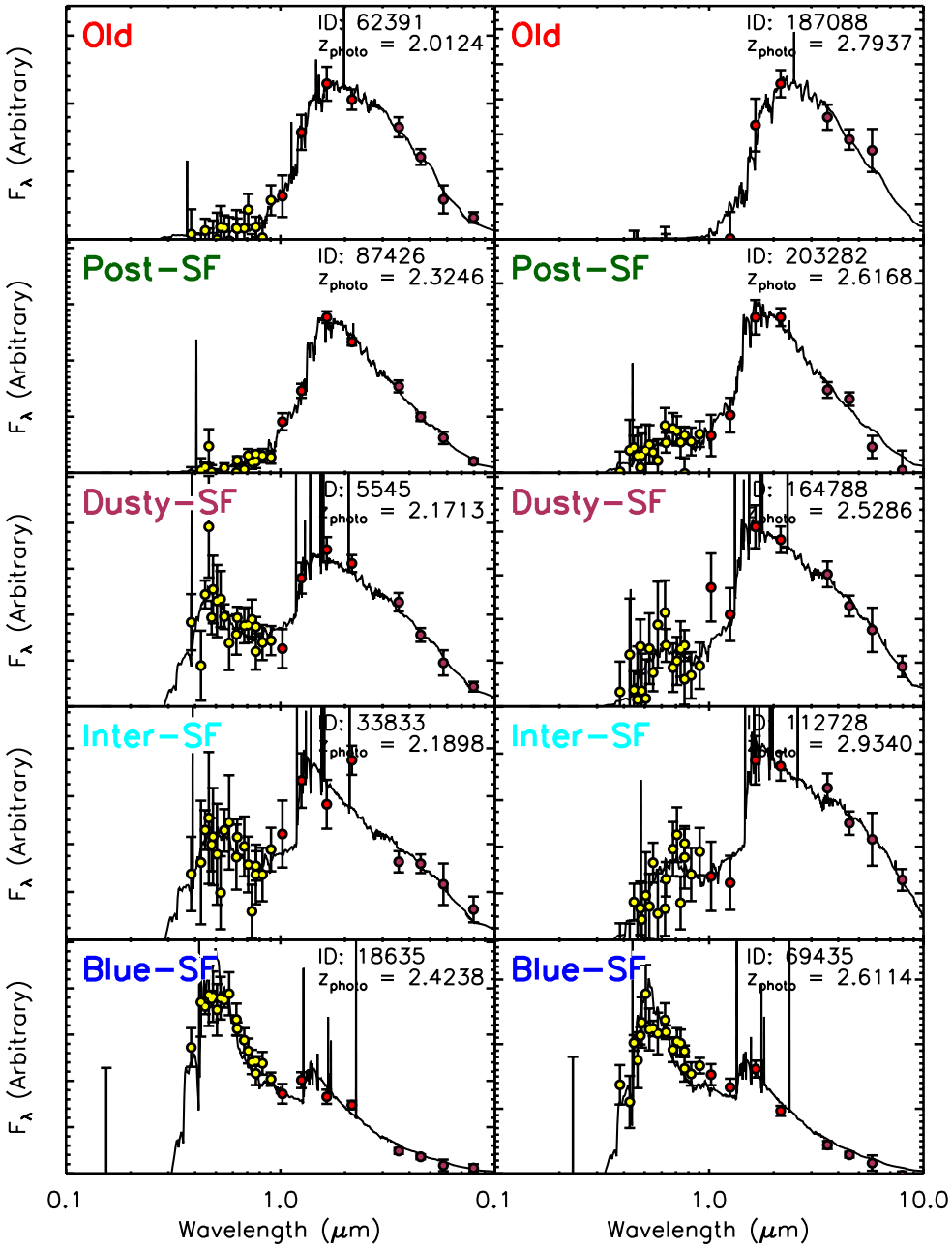

Figure 12. Same as Figure 10 but for galaxies at $2 < z < 3$.
(A color version of this figure is available in the online journal.)

To determine the $L_{\rm IR}$, we extrapolate the measured 24 μm flux using templates. The Chary & Elbaz (2001) and Dale & Helou (2002) models are based on local galaxy templates calibrated using *IRAS* and implicitly assume a correlation between $L_{\rm IR}$ and the dust temperature (T_d). As has been discussed in recent papers, it appears that this correlation may not hold up to the highest redshifts (e.g., Muzzin et al. 2010; Elbaz et al. 2010). Instead of using the luminosity-dependent templates, we use a single template to determine $L_{\rm IR}$ for all galaxies. This approach has been advocated by many recent studies (e.g., Wuyts et al. 2008; Muzzin et al. 2010; Elbaz et al. 2010). We use the log-average of the Dale & Helou (2002) templates for this computation (see Wuyts et al. 2008), but note that using the log-average of the Chary & Elbaz (2001) templates would provide very similar results (Muzzin et al. 2010). We list the $L_{\rm IR}$ determined using this method in Table 6.

We convert the L_{2800} into a $\rm SFR_{UV,uncorr}$ using the conversion factor $\rm SFR_{UV,uncorr} = 3.234 \times 10^{-10}\ L_{2800}$ from Kennicutt (1998), adapted to a Kroupa IMF by Bell et al. (2005). We note that this is the observed SFR, and is not corrected for dust-extinction. The $L_{\rm IR}$ is converted into a $\rm SFR_{IR}$ using $\rm SFR_{IR} = 0.98 \times 10^{-10}\ L_{IR}$ from Kennicutt (1998), adapted to a Kroupa IMF by Bell et al. (2005). The total SFR of the galaxy can then be determined via $\rm SFR_{tot} = SFR_{UV,uncorr} + SFR_{IR}$. These values are also listed in Table 6.

5.6. The Star Formation Main Sequence

Many recent studies have shown evidence for a correlation between the SFR of star-forming galaxies and their $M_{\rm star}$ (e.g., Noeske et al. 2007; Elbaz et al. 2007; Daddi et al. 2007; Wuyts et al. 2011; Whitaker et al. 2012b). This correlation has become

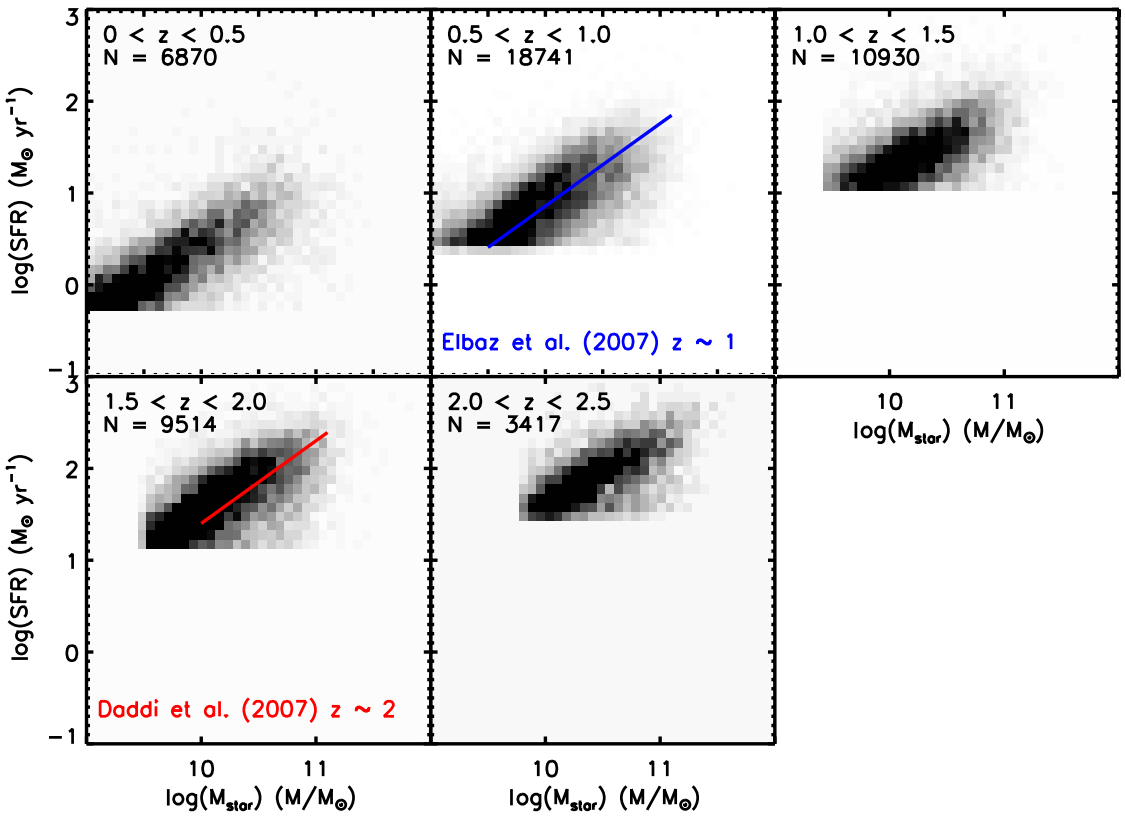

Figure 13. Log(SFR) vs. $M_{\rm star}$ in difference redshift bins for star-forming galaxies selected using the *UVJ* diagram (Figure 9). As in many previous works there is a correlation between the SFR of galaxies and their mass. The blue and red curves are power-law fits to the relations determined by Elbaz et al. (2007) and Daddi et al. (2007) using data from the GOODS survey. The normalization and slope of the star formation main sequence evolves similarly between the two studies.

(A color version of this figure is available in the online journal.)

known as the "star formation main sequence." In Figure 13 we plot gray-scale histograms of the star formation main sequence for star-forming galaxies in the UltraVISTA catalog between $0.0 < z < 2.5$. Star-forming galaxies have been selected by their location in the *UVJ* diagram using the prescriptions defined in Muzzin et al. (2013), which are based on those determined by Williams et al. (2009). The SFRs plotted in Figure 13 are total SFRs which have been computed from $\rm SFR_{tot} = SFR_{UV,uncorr} + SFR_{IR}$. Only sources that have a $>3\sigma$ detection at 24 μm are shown.

Figure 13 shows clearly the existence of a main sequence of star formation for galaxies in the UltraVISTA catalog. As a comparison we plot the power-law fits to the main sequence at $z \sim 1$ and $z \sim 2$ measured by Elbaz et al. (2007) and Daddi et al. (2007), respectively using the GOODS data. There is reasonable agreement between the evolution of the normalization of the relations between the two data sets. There may be slightly different slopes and normalizations, but this may be because the redshift ranges shown in Figure 13 are not exact matches to those in Elbaz et al. (2007) and Daddi et al. (2007). A more detailed look at the star formation main sequence from UltraVISTA will be presented in a future paper.

6. CONCLUSION

In this paper we have presented a public K_s-selected catalog covering 1.62 deg^2 of the COSMOS/UltraVISTA field. The photometric catalog consists of PSF matched photometry in 30 bands and covers the wavelength range 0.15–24 μm. The catalog contains 262,615 sources down to the 3σ limit of $K_s(2\farcs1) < 24.35$, and 179,291 sources down to the 90% completeness limit $K_{s,\rm tot} < 23.4$.

Photometric redshifts have been computed for all galaxies using the EAZY photometric redshift code. Comparison of the $z_{\rm phot}$ with $z_{\rm spec}$ from zCOSMOS and other spectroscopic surveys shows that at $z < 1.5$ the catastrophic outlier fraction is low (1.56%), and the rms scatter is low ($\delta z/(1+z) = 0.013$. The $z_{\rm phot}$ also agree well with $z_{\rm phot}$ determined using the NMBS.

Included with the catalog is a set of $M_{\rm star}$ and stellar population parameters computed using the FAST SED fitting code. These $M_{\rm star}$ show good agreement with those calculated in the NMBS, with only a 0.05 dex systematic difference. Rest-frame $U - V$ and $V - J$ colors are computed for all galaxies. The population of galaxies in the COSMOS/UltraVISTA field shows a clear bi-modality in color–color space up to $z \sim 2$, and thereafter the bi-modality begins to break down.

The catalog contains measures of L_{2800} and $L_{\rm IR}$ as well the inferred SFRs from those parameters. Plotting these against the $M_{\rm star}$ for *UVJ*-selected star-forming galaxies shows that there is a star formation main sequence up to $z \sim 2.5$. The evolution of the main sequence is consistent with previous measurements.

In a companion paper to this one (Muzzin et al. 2013) we show the evolution of the stellar mass functions of galaxies up to $z \sim 4$ using the K_s-selected UltraVISTA catalog. The photometry, photometric redshifts, stellar population parameters, rest-frame colors, and UV and IR SFRs from the K_s-selected catalog are now made available to the astronomical community though the catalog Web site.[9] We hope that it proves to be a useful resource for further galaxy evolution studies.

[9] http://www.strw.leidenuniv.nl/galaxyevolution/ULTRAVISTA/

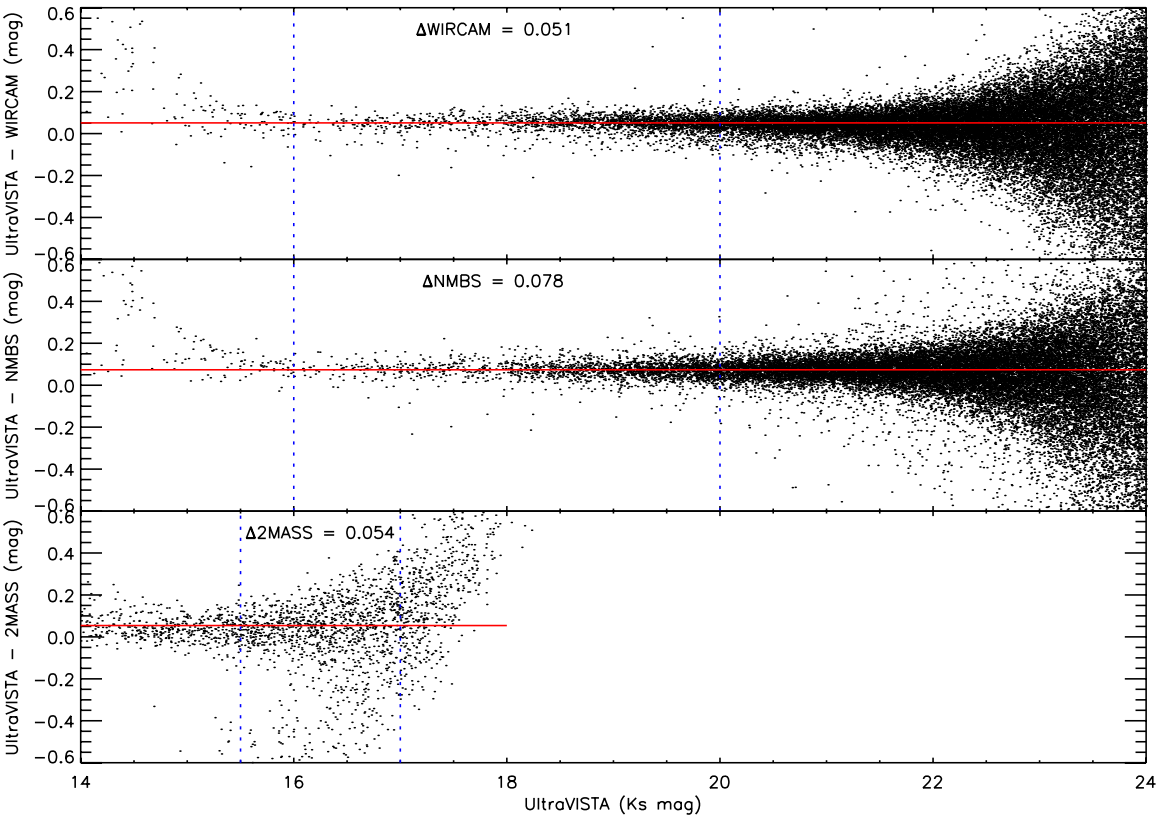

Figure 14. Top two panels: comparison between K_s photometry in UltraVISTA to the K_s and K photometry from WIRCAM and the NMBS. Magnitudes have been measured in a 2.″1 aperture on PSF matched images. Bottom panel: comparison of the UltraVISTA K_s photometry to 2MASS K_s photometry over the full UltraVISTA area. The blue dotted lines indicate the magnitude range used to compute the median offset, and the red solid line shows the median offset. There is a <0.1 mag difference between UltraVISTA and the other surveys; however, UltraVISTA is systematically too faint and so we have elected to redefine the K_s zero point to match the NMBS zero point.

(A color version of this figure is available in the online journal.)

D.M. acknowledges support from a Tufts University Mellon Research Fellowship in Arts and Sciences. B.M.J. and J.P.U.F. acknowledge support from the ERC-StG grant EGGS-278202. The Dark Cosmology Centre is funded by the Danish National Research Foundation. J.S.D. acknowledges the support of the European Research Council through the award of an Advanced Grant, and the support of the Royal Society via a Wolfson Research Merit Award. A.M., D.M., and M.S. thank Gigi Guzzo and the Osservatorio Astronomico di Milano-Merate for the hospitality while working on portions of this research.

APPENDIX

COMPARISON OF UltraVISTA K_s ZERO POINT TO OTHER DATA SETS

In this appendix we make a comparison between the K_s-band photometry between several data sets that cover the COSMOS field to test the photometric zero point of the UltraVISTA K_s imaging. For the catalog, the zero point in K_s is important because K_s is used as the anchor filter when calculating the zero-point offsets in the remaining filters (Section 4.1). We compare the UltraVISTA K_s-band to the K-band imaging from the NMBS (Whitaker et al. 2011), which reaches a 5σ depth of $K = 23.5$. We also compare the CFHT/WIRCAM K_s imaging from McCracken et al. (2010), which in the deepest regions reaches a 5σ depth of $K_s = 23.65$ in a 2″ aperture. Lastly, we compare to sources detected in 2MASS (Skrutskie et al. 2006), although we note that the overlap in dynamic range between UltraVISTA and 2MASS is limited.

For comparison with the WIRCAM and NMBS data we use the region of the survey that is in common to all three data sets. This region covers ∼0.22 deg^2 and is located in the northwest corner of the UltraVISTA field. We perform PSF matching on all three data sets, matching to the worst seeing image, which is the NMBS (∼1.″1). Ten bright unsaturated stars in the region are used in order to determine the convolution kernel. Once the PSFs are homogenized we use SExtractor to find objects on each image individually and measure fluxes within a 2.″1 diameter aperture. Object detection is performed on each image separately because there are small, but noticeable differences in the astrometry between the surveys. If object detection was performed with SExtractor in dual-image mode, small astrometry differences could appear as zero-point differences. Source lists from each catalog are matched using a 0.″5 search radius. Using a small radius means that some matches may be missed, but the tradeoff is that there are few ambiguous matches.

In Figure 14 we plot the comparison of the UltraVISTA K_s photometry versus the WIRCAM and NMBS K_s photometry. In general, the comparison is good. There is a small systematic difference between the surveys; however, there is no systematic difference as a function of magnitude. If we compare the differences in the magnitude range $16 < K_s < 20$, we find an offset between UltraVISTA and WIRCAM of 0.051 mag, and an offset between UltraVISTA and NMBS of 0.078 mag, with UltraVISTA being fainter in both cases.

The difference of 0.054 mag between the UltraVISTA and the WIRCAM data is very similar to that measured by

McCracken et al. (2012; see their Figure 10) for BzK-selected stars in the fields of the two surveys. The difference between UltraVISTA and the NMBS is slightly larger than the difference between UltraVISTA and WIRCAM. That difference implies that the WIRCAM photometry should be 0.027 mag fainter than the NMBS photometry. Indeed, this implied difference is very similar to the actual difference measured by Whitaker et al. (2011) who performed PSF matched photometry between the NMBS and the WIRCAM data (see their Figure 12).

In the bottom panel of Figure 14 we also compare the UltraVISTA photometry to photometry from the 2MASS catalog. For this comparison we do not perform PSF matching, but match objects between the surveys over the full 1.62 deg^2 UltraVISTA field. We compare the total magnitudes measured for UltraVISTA (before any zero-point offset has been applied), to the "default" magnitudes of objects extracted from the 2MASS point source catalog. As Figure 14 shows, there is reasonable agreement; however, the dynamic range over which the comparison can be made is limited. If we compare objects at $15.5 < K_s < 17.0$ we find a systematic difference of 0.054 mag, with again UltraVISTA being slightly fainter.

Although it is not completely clear which zero point is the most trustworthy, these comparisons do suggest that the DR1 UltraVISTA K_s band zero point may be too large at the 0.05–0.08 mag level. In order to provide consistency with our previous work, we have elected to adjust the zero point, making it 0.08 mag brighter so that it matches the NMBS zero point. We note that this offset in zero point does not have a significant impact on the colors in the catalog because the zero point offsets in the other bands are derived relative to the K_s-band. This means that parameters derived from the colors such as the $z_{\rm phot}$ are also unchanged. The best-fit M/L ratios are also unchanged but the scaling of the K_s band means that the $M_{\rm star}$ are systematically changed by adjusting the K_s zero point; however, this change is quite small. The offset of 0.08 mag corresponds to a difference of 0.03 dex in $M_{\rm star}$. If we were to apply the zero point implied by 2MASS or the WIRCAM data, it would imply stellar masses that are only 0.01 dex different than those in the current catalog.

REFERENCES

Aretxaga, I., Wilson, G. W., Aguilar, E., et al. 2011, MNRAS, 415, 3831
Arnouts, S., Walcher, C. J., Le Fèvre, O., et al. 2007, A&A, 476, 137
Bell, E. F., Papovich, C., Wolf, C., et al. 2005, ApJ, 625, 23
Bertin, E., & Arnouts, S. 1996, A&AS, 117, 393
Bezanson, R., van Dokkum, P., van de Sande, J., Franx, M., & Kriek, M. 2013, ApJL, 764, L8
Bielby, R., Hudelot, P., McCracken, H. J., et al. 2012, A&A, 545, A23
Bower, R. G., Benson, A. J., & Crain, R. A. 2012, MNRAS, 422, 2816
Brammer, G. B., van Dokkum, P. G., & Coppi, P. 2008, ApJ, 686, 1503
Brammer, G. B., van Dokkum, P. G., Franx, M., et al. 2012, ApJS, 200, 13
Brammer, G. B., Whitaker, K. E., van Dokkum, P. G., et al. 2009, ApJL, 706, L173
Brammer, G. B., Whitaker, K. E., van Dokkum, P. G., et al. 2011, ApJ, 739, 24
Bruzual, G., & Charlot, S. 2003, MNRAS, 344, 1000
Bundy, K., Ellis, R. S., Conselice, C. J., et al. 2006, ApJ, 651, 120
Calzetti, D., Armus, L., Bohlin, R. C., et al. 2000, ApJ, 533, 682
Capak, P., Aussel, H., Ajiki, M., et al. 2007, ApJS, 172, 99
Caputi, K. I., Cirasuolo, M., Dunlop, J. S., et al. 2011, MNRAS, 413, 162
Chabrier, G. 2003, PASP, 115, 763
Chary, R., & Elbaz, D. 2001, ApJ, 556, 562
Cirasuolo, M., McLure, R. J., Dunlop, J. S., et al. 2010, MNRAS, 401, 1166
Daddi, E., Dickinson, M., Morrison, G., et al. 2007, ApJ, 670, 156
Daddi, E., Renzini, A., Pirzkal, N., et al. 2005, ApJ, 626, 680
Dale, D. A., & Helou, G. 2002, ApJ, 576, 159
Elbaz, D., Daddi, E., Le Borgne, D., et al. 2007, A&A, 468, 33
Elbaz, D., Hwang, H. S., Magnelli, B., et al. 2010, A&A, 518, L29
Elvis, M., Civano, F., Vignali, C., et al. 2009, ApJS, 184, 158
Fioc, M., & Rocca-Volmerange, B. 1999, arXiv:9912179
Fontanot, F., De Lucia, G., Monaco, P., Somerville, R. S., & Santini, P. 2009, MNRAS, 397, 1776
Förster Schreiber, N. M., van Dokkum, P. G., Franx, M., et al. 2004, ApJ, 616, 40
Franx, M., Labbé, I., Rudnick, G., et al. 2003, ApJL, 587, L79
Frayer, D. T., Sanders, D. B., Surace, J. A., et al. 2009, AJ, 138, 1261
Grogin, N. A., Kocevski, D. D., Faber, S. M., et al. 2011, ApJS, 197, 35
Guo, Q., White, S., Boylan-Kolchin, M., et al. 2011, MNRAS, 413, 101
Hasinger, G., Cappelluti, N., Brunner, H., et al. 2007, ApJS, 172, 29
Henriques, B. M. B., White, S. D. M., Lemson, G., et al. 2012, MNRAS, 421, 2904
Ilbert, O., Arnouts, S., McCracken, H. J., et al. 2006, A&A, 457, 841
Ilbert, O., Capak, P., Salvato, M., et al. 2009, ApJ, 690, 1236
Ilbert, O., Salvato, M., Le Floc'h, E., et al. 2010, ApJ, 709, 644
Kennicutt, R. C., Jr. 1998, ARA&A, 36, 189
Koekemoer, A. M., Aussel, H., Calzetti, D., et al. 2007, ApJS, 172, 196
Koekemoer, A. M., Faber, S. M., Ferguson, H. C., et al. 2011, ApJS, 197, 36
Kriek, M., Labbé, I., Conroy, C., et al. 2010, ApJL, 722, L64
Kriek, M., van Dokkum, P. G., Labbé, I., et al. 2009, ApJ, 700, 221
Kron, R. G. 1980, ApJS, 43, 305
Labbé, I., Franx, M., Rudnick, G., et al. 2003, AJ, 125, 1107
Labbé, I., González, V., Bouwens, R. J., et al. 2010, ApJL, 716, L103
Labbé, I., Huang, J., Franx, M., et al. 2005, ApJL, 624, L81
Labbé, I., Oesch, P. A., Bouwens, R. J., et al. 2012, arXiv:1209.3037
Lawrence, A., Warren, S. J., Almaini, O., et al. 2007, MNRAS, 379, 1599
Lilly, S. J., Le Brun, V., Maier, C., et al. 2009, ApJS, 184, 218
Lilly, S. J., Le Fèvre, O., Renzini, A., et al. 2007, ApJS, 172, 70
Maíz Apellániz, J. 2006, AJ, 131, 1184
Maraston, C. 2005, MNRAS, 362, 799
Maraston, C., Pforr, J., Renzini, A., et al. 2010, MNRAS, 407, 830
Marchesini, D., Stefanon, M., Brammer, G. B., & Whitaker, K. E. 2012, ApJ, 748, 126
Marchesini, D., van Dokkum, P. G., Förster Schreiber, N. M., et al. 2009, ApJ, 701, 1765
Marchesini, D., Whitaker, K. E., Brammer, G., et al. 2010, ApJ, 725, 1277
Martin, D. C., Fanson, J., Schiminovich, D., et al. 2005, ApJL, 619, L1
McCracken, H. J., Capak, P., Salvato, M., et al. 2010, ApJ, 708, 202
McCracken, H. J., Milvang-Jensen, B., Dunlop, J., et al. 2012, A&A, 544, A156
McLure, R. J., Cirasuolo, M., Dunlop, J. S., et al. 2006, MNRAS, 372, 357
Muzzin, A., Marchesini, D., Stefanon, M., et al. 2013, arXiv:1303.4409
Muzzin, A., van Dokkum, P., Kriek, M., et al. 2010, ApJ, 725, 742
Noeske, K. G., Weiner, B. J., Faber, S. M., et al. 2007, ApJL, 660, L43
Oliver, S. J., Bock, J., Altieri, B., et al. 2012, MNRAS, 424, 1614
Onodera, M., Renzini, A., Carollo, M., et al. 2012, ApJ, 755, 26
Papovich, C., Finkelstein, S. L., Ferguson, H. C., Lotz, J. M., & Giavalisco, M. 2011, MNRAS, 412, 1123
Patel, S. G., Holden, B. P., Kelson, D. D., et al. 2012, ApJL, 748, L27
Patel, S. G., van Dokkum, P. G., Franx, M., et al. 2013, ApJ, 766, 15
Quadri, R., van Dokkum, P., Gawiser, E., et al. 2007, ApJ, 654, 138
Sanders, D. B., Salvato, M., Aussel, H., et al. 2007, ApJS, 172, 86
Schinnerer, E., Sargent, M. T., Bondi, M., et al. 2010, ApJS, 188, 384
Schinnerer, E., Smolčić, V., Carilli, C. L., et al. 2007, ApJS, 172, 46
Schlegel, D. J., Finkbeiner, D. P., & Davis, M. 1998, ApJ, 500, 525
Scott, K. S., Austermann, J. E., Perera, T. A., et al. 2008, MNRAS, 385, 2225
Scoville, N., Aussel, H., Brusa, M., et al. 2007, ApJS, 172, 1
Skrutskie, M. F., Cutri, R. M., Stiening, R., et al. 2006, AJ, 131, 1163
Taniguchi, Y., Scoville, N., Murayama, T., et al. 2007, ApJS, 172, 9
van de Sande, J., Kriek, M., Franx, M., et al. 2011, ApJL, 736, L9
van de Sande, J., Kriek, M., Franx, M., et al. 2013, ApJ, submitted (arXiv:1211.3424)
van Dokkum, P. G., Labbé, I., Marchesini, D., et al. 2009, PASP, 121, 2
van Dokkum, P. G., Quadri, R., Marchesini, D., et al. 2006, ApJL, 638, L59
Whitaker, K. E., Kriek, M., van Dokkum, P. G., et al. 2012a, ApJ, 745, 179
Whitaker, K. E., Labbé, I., van Dokkum, P. G., et al. 2011, ApJ, 735, 86
Whitaker, K. E., van Dokkum, P. G., Brammer, G., & Franx, M. 2012b, ApJL, 754, L29
Williams, R. J., Quadri, R. F., Franx, M., van Dokkum, P., & Labbé, I. 2009, ApJ, 691, 1879
Wuyts, S., Förster Schreiber, N. M., van der Wel, A., et al. 2011, ApJ, 742, 96
Wuyts, S., Labbé, I., Franx, M., et al. 2007, ApJ, 655, 51
Wuyts, S., Labbé, I., Schreiber, N. M. F., et al. 2008, ApJ, 682, 985